

Rochelle salt-based biodegradable piezoelectric devices for nerve regeneration and intestinal motility monitoring

Received: 23 June 2025

Accepted: 7 January 2026

Published online: 29 January 2026

 Check for updates

Fanqi Dai^{1,2,19}, Haofeng Cheng^{3,4,5,6,7,19}, Hui Qi^{8,19}, Honglai Cai⁹, Abdul Aziz^{1,2}, Tianqi Su^{4,5,6,7}, Yanjun Guan^{4,5,6}, Yuhui Cui^{4,5,6,7}, Jingwei Meng^{4,5,6}, Handi Deng^{10,11,12,13}, Qianxi Wu¹⁴, Yongsheng Jie⁸, Lei Chen⁸, Sixu Wang^{1,15}, Tianyi Feng^{1,15}, Wei Li^{1,15}, Fei You¹⁰, Shengnan Liu^{1,2}, Bingbing Yu^{1,2}, Can Yang^{1,2}, Jiang Peng^{4,5,6}, Xing Sheng^{10,11,12,16,17}, Jing-feng Li^{1,15}, Milin Zhang¹⁰, Qian Li^{1,15}, Cheng Ma^{10,11,12,13}, Lei Tian¹⁸, Jun Zhang^{3,7}, Yu Wang^{4,5,6} & Lan Yin^{1,2,17}

Piezoelectric materials provide a unique platform for bioelectronic interfaces, enabling dynamic sensing and electroactive therapies through bidirectional transduction between biomechanical and bioelectrical signals. However, the development of bioresorbable piezoelectric materials that combine high functional performance with mechanical compliance remains a critical challenge for seamless integration with soft biological tissues, while eliminating the need for retrieval surgeries and long-term material retention. Here, we report a bioresorbable, flexible piezoelectric composite composed of Rochelle salt (RS) crystals embedded within poly(L-lactic acid) (PLLA) nanofibers. Fabricated via electrospinning and uniaxial compression, centimeter-scale biodegradable nanofiber films are achieved, exhibiting excellent effective piezoelectric coefficient of 43.1 pC N⁻¹ and piezoelectric voltage coefficient of 1909.2 mV m N⁻¹, surpassing the piezoelectric performance of previously reported biodegradable flexible materials. Ultrasound-driven scaffold devices derived from these bioresorbable piezoelectric materials markedly enhance sciatic nerve regeneration in rodents. Additionally, a biodegradable piezoelectric strain sensor enables wireless, real-time monitoring of intestinal motility, facilitating diagnosis of colonic dysfunction. Together, these findings establish a prominent materials paradigm for biodegradable piezoelectric electronics, offering a versatile platform for bioelectronic applications in regenerative medicine, neuromodulation, and physiological monitoring.

Implantable bioelectronics leveraging piezoelectric materials enable mechanical-electrical coupling and have facilitated diverse biomedical applications, including energy harvesting¹⁻³, tumor therapy^{4,5}, tissue regeneration^{6,7}, drug delivery⁸⁻¹⁰, biosensing^{11,12}, etc. However,

commonly used piezoelectric materials, such as Lead Zirconate Titanate (PZT)^{13,14}, Barium Titanate Oxide (BTO)¹⁵⁻¹⁷, Lithium Niobate (LN)¹⁸, Potassium Sodium Niobate (KNN)^{19,20}, and Polyvinylidene Fluoride (PVDF)^{21,22}, are either non-biodegradable or contain bio-toxic

A full list of affiliations appears at the end of the paper. ✉ e-mail: tianmushroom@163.com; zhangjun@301hospital.com.cn; wangyu@301hospital.com.cn; lanyin@tsinghua.edu.cn

constituents, necessitating complex surgical procedures for device removal to avoid long-term material retention and minimize potential toxic effects^{8,23}. Retrieval surgery is often complicated by fibrotic encapsulation, a common outcome of foreign body reactions, which can result in secondary tissue damage. Emerging biodegradable piezoelectric materials capable of safe degradation in physiological environments present opportunities to eliminate infection risks and tissue trauma associated with surgical removal. Reported biodegradable piezoelectric materials include amino acid crystals (e.g., glycine^{24,25}, DL-alanine²⁶ and diphenylalanine^{27–29}), proteins (e.g., silk³⁰ and collagen³¹), polysaccharides (e.g., chitosan^{32,33}, chitin³⁴ and cellulose^{35,36}), and synthetic polymers (e.g., poly(L-lactide) (PLLA)^{37,38} and Poly-3-hydroxybutyrate (PHB)³⁹). The piezoelectric properties of these materials originate from dipole alignment due to non-centrosymmetric crystal structures, molecular strain and hierarchical organization^{40,41}. As the piezoelectric properties of biodegradable materials are often weak compared with inorganic materials, several strategies have been developed to enhance their piezoelectric response, including directional stretching⁴², electrospinning^{43,44}, electrical poling^{36,45,46} and self-assembly processes driven by intermolecular forces^{38,47–49}. In addition, high piezoelectric coefficients have been achieved through the design of molecular crystals⁴⁹. Despite these advancements, critical challenges remain. Most biodegradable piezoelectric materials exhibit lower longitudinal piezoelectric coefficients relative to their shear coefficients, necessitating complex device architectures or sophisticated processing techniques to offset performance limitations. Moreover, high-performance piezoelectric materials typically exhibit high crystallinity, and efforts to enhance their flexibility often come at the expense of piezoelectric performance, thereby limiting their versatile application in bioelectronic interfaces with soft tissues.

Rochelle salt (RS, $\text{NaKC}_4\text{H}_4\text{O}_6 \cdot 4\text{H}_2\text{O}$) represents an alternative piezoelectric material based on organic molecules^{50,51}, featuring strong piezoelectric response (d_{14} reaching up to 2300 pm V^{-1})⁵² and excellent biocompatibility as a Food and Drug Administration (FDA) approved food additive (E337). While RS was historically employed in microphones and sensors, its inherent instability led to its discontinuation in conventional electronics. However, the water-solubility of RS now offers unique opportunities to develop high-performance biodegradable electronic devices. Recently, in pursuit of environmentally friendly applications, a few studies have explored the integration of RS with natural materials such as wood^{53,54} and paper⁵⁵, or with 3D-printed structures^{56,57}, through strategies promoting directional crystal growth. Nevertheless, insufficient flexibility and limited piezoelectric performance constrain their potential applications. Moreover, the inherent hygroscopicity and brittleness of RS have thus far precluded its use in the development of high-performance implantable bioelectronics.

In this study, we propose biodegradable, flexible and piezoelectric nanofiber films based on micro-sized RS crystalline and PLLA polymers, through the combination of electrospinning and mechanical compression. The centimeter-scale nanofiber film exhibits desirable flexibility and a high effective piezoelectric coefficient (maximum $d_{33\text{eff}} = 43.1 \pm 3.0 \text{ pC N}^{-1}$), representing over a tenfold enhancement compared to pure PLLA fibers and exceeding the piezoelectric performance of previously reported biodegradable flexible piezoelectric materials. The piezoelectric material also exhibits a large piezoelectric voltage coefficient (g_{33}) of $1909.2 \text{ mV m N}^{-1}$, indicating exceptional voltage-generating capability that surpasses not only reported biodegradable piezoelectric materials but also many non-degradable counterparts. Based on bioresorbable piezoelectric nanofibers, we successfully develop an ultrasound (US) responsive scaffold device for sciatic nerve regeneration and a strain sensor system for monitoring intestinal peristalsis (Fig. 1a). This work provides insights for biodegradable piezoelectric electronics as a key

platform for wireless regenerative electrotherapy and real-time diagnostic monitoring.

Results

Fabrication and characterization of RS-based nanofibers

Micron-sized RS crystal particles are obtained by mechanically ball milling the as-received RS crystals, and corresponding X-ray diffraction (XRD) and Fourier transform infrared (FTIR) spectroscopy analyses (Supplementary Fig. 1a, b) indicate that the chemical composition remains unchanged after grinding. To achieve optimal piezoelectric properties and mechanical flexibility, micron-sized RS crystal particles are incorporated into a PLLA precursor solution with a PLLA to RS mass ratio of 4:1, and electrospun into PLLA/RS nanofibers (PLLA/RS), followed by vertical uniaxial compression (30 kN unless otherwise specified) to form densely packed nanofibers (PRSC) (Supplementary Fig. 2a). The optical images of resulting centimeter-scale flexible PLLA/RS and PRSC films appear in Supplementary Fig. 2b, c. Scanning electron microscopy (SEM) images reveal the surface morphology of PLLA/RS and PRSC films, showing RS crystals embedded within the aligned PLLA fibers (Fig. 1b and Supplementary Fig. 2d). Fiber diameter and RS crystal particle size are measured using ImageJ based on SEM images. The PLLA/RS film has a fiber diameter of $0.17 \pm 0.06 \mu\text{m}$ and an RS crystal particle size of $1.01 \pm 0.49 \mu\text{m}$, and the PRSC film has a fiber diameter of $0.19 \pm 0.06 \mu\text{m}$ and an RS crystal particle size of $0.96 \pm 0.43 \mu\text{m}$. No significant differences in fiber diameter or RS crystal particle size are observed between the two types of films. Energy-dispersive spectroscopy (EDS) mapping confirms the presence of RS crystals through the distribution of characteristic elements, sodium (Na) and potassium (K) (Fig. 1b). The porosity of the PRSC film decreases compared to the PLLA/RS film (Supplementary Fig. 2e), which is expected to improve dipole density and improve piezoelectric performance, as will be discussed later. To evaluate the loading efficiency of RS in PRSC fibers, we compare the thermogravimetric curves of PRSC, PLLA nanofibers, and RS crystals (Supplementary Fig. 2f). Pure RS crystals and PRSC exhibit a rapid weight loss between 50–120 °C, corresponding to the release of water of crystallization. At 370 °C, RS crystals retain $52.9\% \pm 0.3\%$ of their mass, consistent with previous reports⁵⁸. In contrast, PLLA decomposes rapidly between 250–330 °C, leaving $3.7\% \pm 0.1\%$ residue, whereas PRSC shows a higher residue of $13.3\% \pm 0.3\%$. Based on these characteristics, the RS content in PRSC is calculated to be $19.5\% \pm 0.6\%$, closely matching the initial feeding ratio of PLLA to RS (4:1). This corresponds to a loading efficiency of $\sim 97.5\%$, indicating that the RS content remains consistent after electrospinning and post-processing. Figure 1c displays the FTIR spectrum of PLLA/RS nanofibers, compared with pure RS crystals (RS) and electrospun PLLA nanofibers (PLLA). The composite PLLA/RS nanofibers exhibit a characteristic peak at 1600 cm^{-1} corresponding to the carboxylate anion structure of RS crystals⁵⁸. Moreover, we investigate the influence of the PLLA to RS mass ratio on electrospun nanofibers. The results suggest that increasing the RS content leads to RS crystal agglomeration (Supplementary Fig. 3a). Additionally, improved fiber alignment is observed with increasing drum rotation speed during electrospinning, as reflected by the Herman orientation factor rising from 0.251 ± 0.093 at 400 rpm to 0.767 ± 0.029 at 2800 rpm (Supplementary Fig. 3b), which may contribute to enhanced piezoelectric performance. A PLLA to RS mass ratio of 4:1 and a drum rotation speed of 2800 rpm are subsequently selected to fabricate piezoelectric thin films, unless otherwise specified.

To investigate the effects of electrospinning and mechanical compression on RS crystal orientation, XRD analysis is performed on PRSC, PLLA/RS nanofibers (without mechanical compression), solvent-casted PLLA/RS films (without electrospinning), RS crystals, and PLLA nanofibers (Fig. 1d). The normalized XRD spectra show that the solvent-casted PLLA/RS film displays polycrystalline patterns similar to RS powder, while the PRSC and PLLA/RS nanofibers exhibit enhanced

Fig. 1 | Fully biodegradable and flexible piezoelectric nanofibers based on Rochelle salt (RS) and poly (L-lactic acid) (PLLA). **a** Schematic illustration of the fully biodegradable piezoelectric PRSC composites for ultrasound-driven peripheral nerve regeneration and wireless colon peristalsis sensing. **b** SEM images of PLLA/RS nanofibers (PLLA to RS mass ratio of 4:1) and PLLA/RS after compression (PRSC), with EDS mapping demonstrating the presence of sodium and potassium from the RS crystals. **c** FTIR spectra of RS crystal powder (RS), electrospun PLLA nanofibers (PLLA) and PLLA/RS (4:1) nanofibers. a.u. in this figure and all subsequent figures represents arbitrary units. **d** XRD spectra of the PRSC nanofibers, PLLA/RS (4:1) nanofibers, solvent-casted PLLA/RS (4:1) films, RS crystal powders

and PLLA nanofibers. **e** Pole diagrams of the (310) and (321) planes of RS crystals in different films, including solvent-casted PLLA/RS (4:1) films before and after compression, and PLLA/RS (4:1) nanofibers before and after compression. **f** Stress-strain curves of PLLA nanofibers, PLLA/RS nanofibers with different PLLA to RS mass ratios, and PRSC nanofibers. **g** Young's modulus of different films. **h** Degradation process of the PRSC film in PBS at 65 °C, with the residual mass quantified at different time points. In **g** and **h**, the data are shown as mean \pm s.d. In **b–h**, $n = 3$ independent experiments. $n = 3$ independent experiments. The SPSS software package (version 26.0) is used for the statistical analysis, followed by one-way ANOVA Tukey test (two-sided) ($P < 0.05$, $^{*}P < 0.01$, $^{***}P < 0.001$, $^{****}P < 0.0001$).

RS crystals within highly aligned PLLA fibers, enabling mechanical compression to effectively modulate crystal orientation. Moreover, two-dimensional wide-angle X-ray scattering (2D WAXS) is employed to further investigate the in-plane orientation of PRSC nanofibers (Supplementary Fig. 4a). As the drum rotation speed increases from 400 to 2800 rpm, the WAXS patterns of PRSC evolve from full Debye rings (random orientation) to partial arcs, reflecting increasing alignment of PLLA fibers and RS crystals, consistent with the previously shown SEM results (Supplementary Fig. 3b). Scattering angle (2θ) integration profiles (Supplementary Fig. 4b) display characteristic peaks consistent with the aforementioned XRD results (Fig. 1d), while azimuthal (φ) integration (Supplementary Fig. 4c) reveals enhanced in-plane preferred orientation of the RS (310) and (320) planes at higher drum speeds. Under these conditions, the dipoles exhibit a more ordered in-plane alignment, which contributes to increased polarization of the RS particles. Overall, these results suggest that electrospinning combined with mechanical compression effectively promotes a uniform distribution of RS crystals within aligned PLLA nanofibers and induces a preferred out-of-plane and in-plane orientation of RS crystals, which is expected to improve the piezoelectric response.

The incorporation of micron-sized RS crystals into PLLA nanofibers imparts desirable flexibility compared to the brittleness of pure RS crystals. Figure 1f, g show the tensile stress-strain curves and tensile modulus of PLLA/RS nanofibers with varying RS content. The tensile modulus of the PLLA/RS nanofibers ranges from 20 to 50 MPa. PRSC, obtained by compressing the PLLA/RS (4:1) nanofibers, exhibits enhanced ductility and a tensile modulus of approximately 81 MPa, retaining desirable flexibility. The modulus of PRSC is much lower than that of bulk RS crystals (10–18 GPa)⁵⁵, which minimizes mechanical irritation when interfaces with biological tissues. Moreover, PRSC films demonstrate excellent biodegradability. Accelerated degradation tests show complete degradation in phosphate-buffered saline (PBS) at 65 °C (Fig. 1h). The residual mass ratio gradually decreases over time. At the early stage, degradation is primarily the dissolution of RS crystals. As time progresses, hydrolysis of the PLLA substrate becomes prominent, leading to a more rapid decline in the residual mass ratio. Notably, after 48 days, the material is completely degraded in PBS. Encapsulation with biodegradable polymers can be used to tailor degradation rates and achieve desired functional lifespans, as discussed in a later section.

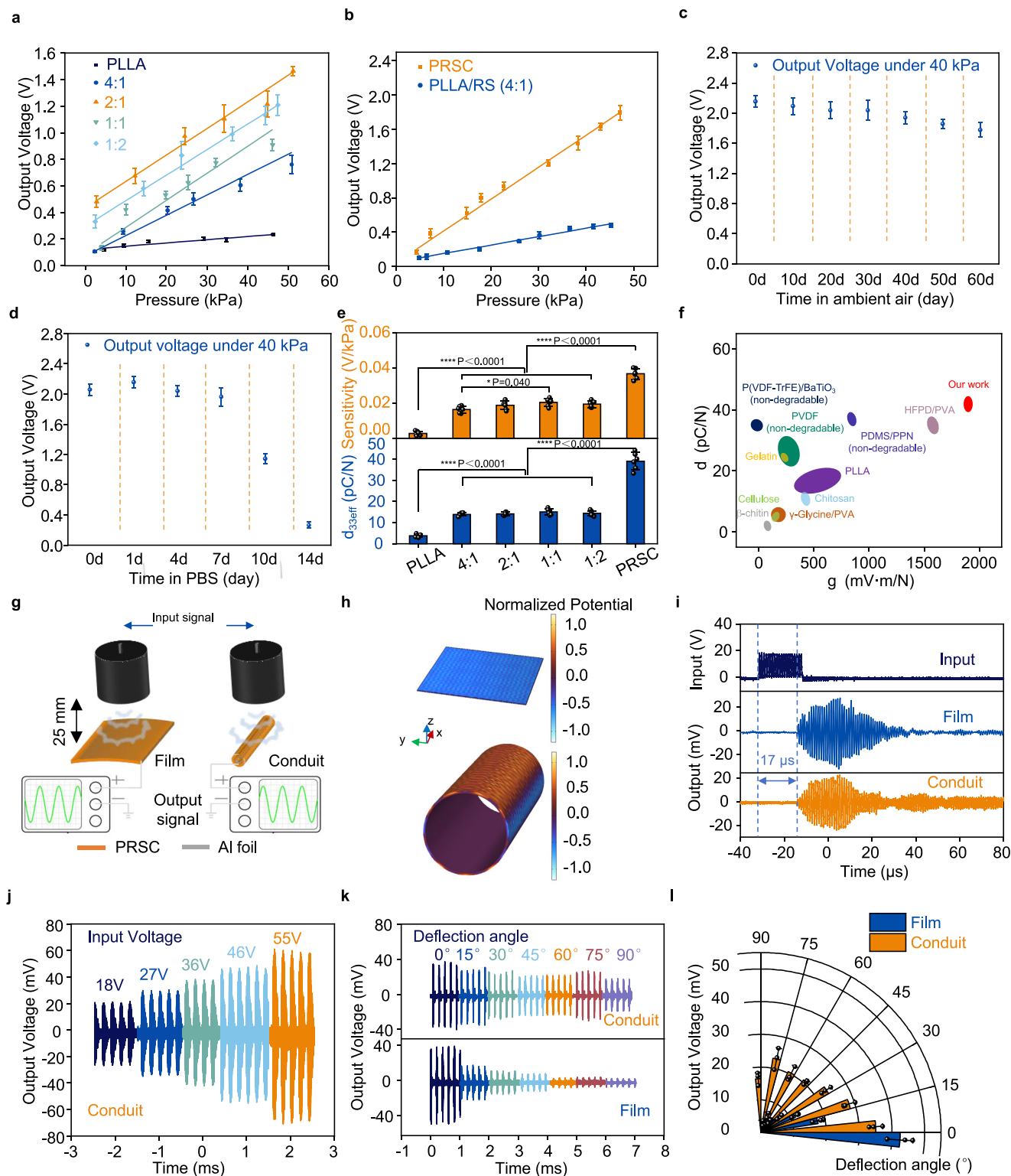
Piezoelectric properties of RS-based nanofibers

Multiple methods are employed to evaluate the piezoelectric performance of RS-based nanofibers. Impact tests are adopted to measure open-circuit voltage and charge output under cyclic loading (Supplementary Fig. 5a). Under a periodic pressure of 3 Hz, the longitudinal open-circuit voltage of PLLA/RS nanofibers exhibits a linear relationship with applied pressure (Fig. 2a), with a sensitivity of 16.2 ± 3.4 mV kPa⁻¹, greater than that of PLLA nanofibers (2.4 ± 1.3 mV kPa⁻¹). Increasing the RS content does not significantly enhance sensitivity, likely due to the agglomeration of polycrystalline RS in the films, as shown earlier (Supplementary Fig. 3a). PRSC

obtained via uniaxial compression demonstrates a ~2.3-fold increase in piezoelectric sensitivity (37.3 ± 3.0 mV kPa⁻¹) (Fig. 2b). Reversing the connecting electrodes during measurement results in voltage outputs of similar magnitude but opposite polarity (Supplementary Fig. 5b), confirming that the signal primarily originates from the piezoelectric effect rather than potential artifact signals. A ring heater coupled with a thermocouple is used to investigate the effects of temperature. At an impact pressure of ~40 kPa, the voltage output at 38 °C is comparable to that at room temperature (Supplementary Fig. 5c), indicating the RS-based piezoelectric materials are suitable for use at physiological temperature (~37 °C). The PRSC films demonstrate stable output over 40,000 loading cycles (Supplementary Fig. 5d). Moreover, PRSC films cut at different angles exhibit similar longitudinal voltage sensitivities (Supplementary Fig. 5e), suggesting that the primary source of piezoelectricity is the embedded RS crystals, rather than the PLLA nanofibers, which have previously been shown to exhibit cutting-angle-dependent piezoelectric responses⁴³.

The long-term stability of PRSC nanofibers encapsulated with a biodegradable PLCL film (~100 μ m) is evaluated in both ambient air and PBS. The encapsulated PRSC retains over 75% of its original open-circuit voltage in ambient air for more than two months (Fig. 2c), and maintains stable output for approximately 7 days in PBS at 37 °C before gradually losing piezoelectric response by day 14 (Fig. 2d). In contrast, the unencapsulated PRSC film gradually loses its piezoelectric output after 10 days of immersion in deionized (DI) water at 37 °C (Supplementary Fig. 5f). We further quantify the RS crystal content in PRSC at different degradation stages using thermogravimetric analysis. The RS mass percentage remains above 25% of the initial value within the first 4 days and is almost completely dissolved by day 10 (Supplementary Fig. 5g). Corresponding XRD spectra (Supplementary Fig. 5h) shows the disappearance of RS crystal peaks after 10 days, along with reduced PLLA crystallinity due to hydrolysis. These results suggest that PLLA fibers provide partial protection against RS dissolution, while the addition of an encapsulation layer further extends operational lifespan.

A quasi-static d_{33} tester is used to characterize the out-of-plane piezoelectric coefficients of RS-based nanofibers (Fig. 2e). PLLA/RS nanofibers with different PLLA to RS mass ratios exhibit similar effective piezoelectric constant $d_{33\text{eff}}$ (13.9–14.4 pC N⁻¹), which are significantly higher than that of pure PLLA nanofibers (3.7 ± 0.6 pC N⁻¹). PRSC demonstrates the highest $d_{33\text{eff}}$ of 39.2 ± 4.1 pC N⁻¹, likely due to the preferred out-of-plane crystal orientation and enhanced dipole density induced by electrospinning and mechanical compression. The $d_{33\text{eff}}$ of PRSC is consistent with the value calculated from output charge measured during impact tests, and the output charge increases with rising cyclic force frequency under low-frequency conditions (Supplementary Fig. 5i–k). The effects of drum rotation speed during electrospinning and applied compression force are also investigated (Supplementary Fig. 6). The results indicate that lower rotation speeds yield lower piezoelectric coefficients, while solvent-casted films exhibit the lowest values (5.7 ± 0.8 pC N⁻¹), likely due to reduced preferred crystal orientation and structural non-uniformity (Supplementary Fig. 6a, b). Within the compression force range of 0–30 kN, the



piezoelectric performance of PLLA/RS nanofibers increases markedly with rising force; beyond 30 kN, further loading continues to enhance the piezoelectric response slightly, reaching a maximum $d_{33\text{eff}}$ of 43.1 ± 3.0 pC N⁻¹ at 100 kN (Supplementary Fig. 6c). Overall, RS-based nanofibers fabricated via electrospinning and mechanical compression exhibit more than a 10-fold increase in piezoelectric performance compared to PLLA nanofibers and an 8-fold increase compared to solvent-casted PLLA/RS films.

A 3D scanning vibrometer is employed to measure the converse piezoelectric coefficient (Supplementary Fig. 7a, b). PRSC exhibits an

average $d_{33\text{eff}}$ of 41.4 ± 10.0 pm V⁻¹, significantly higher than that of PLLA/RS nanofibers (10.1 ± 1.4 pm V⁻¹) (Supplementary Fig. 7c), which is consistent with the measurement by the quasi-static d_{33} tester. Non-uniform distribution of $d_{33\text{eff}}$ is observed (Supplementary Fig. 7b), likely due to the dispersion of RS crystals. It is noted that regions blocked by the measuring probe (yellow dashed boxes in Supplementary Fig. 7b) are excluded from calculating average $d_{33\text{eff}}$. The converse piezoelectric response remains stable under varying AC drive voltages (1 kHz, Supplementary Fig. 7d) and DC bias fields (Supplementary Fig. 7e), confirming measurement accuracy and indicating

Fig. 2 | Piezoelectric characteristics of the fully biodegradable

piezoelectric films. **a** Longitudinal output voltage of PLLA/RS nanofibers and pure PLLA nanofibers under different pressures. **b** Longitudinal output voltage of PLLA/RS (4:1) films and PRSC under different pressures. **c** Longitudinal output voltage of a PRSC film (encapsulated by a PLCL film of 100 μm) under 40 kPa vertical pressure in ambient air at different time points. **d** Longitudinal output voltage of a PRSC film (encapsulated by a PLCL film of 100 μm) under 40 kPa vertical pressure at different time points when soaked in PBS at 37 °C. **e** Effective longitudinal piezoelectric coefficient ($d_{33\text{eff}}$) and sensitivity of different piezoelectric films. **f** Comparison of piezoelectric coefficient (**d**) of representative flexible piezoelectric materials (PVDF⁵⁹, P(VDF-TrFE)/BaTiO₃⁶⁰, PLLA^{42,43}, PDMS/PPN⁶¹, HFDP/PVA⁴⁹, cellulose⁶², chitosan film⁶³, gelatin⁶⁴, β -chitin⁶⁵, γ -glycine/PVA⁴⁷ and our work (PRSC)) versus piezoelectric voltage coefficient (**g**). A complete comparison list is given in supplementary Table 1. **g** Schematic illustration of the experimental set-up of US-

driven output of PRSC devices in the film and conduit formats. **h** Finite element analysis of the distribution of US-driven electric potential of the film and conduit geometry. Ultrasound input: 1 MHz and 1 W cm^{-2} . **i** The input voltage of the US transducer and the output voltage generated by the PRSC film and PRSC conduit measured in DI water at a distance of 25 mm from the US probe. Ultrasound setup: 1 MHz and 18 V input voltage. **j** Output voltage of the PRSC conduit under different US input voltages (1 MHz). **k, l** US response and output voltage of the PRSC film and conduit as a function of the deflection angle from the perpendicular position of the US probe. Ultrasound setup: 1 MHz and 36 V input voltage. In **a–e**, the data are shown as mean \pm s.d. $n = 6$ independent experiments. In **l**, the data are shown as mean \pm s.d. $n = 3$ independent experiments. The SPSS software package (version 26.0) is used for the statistical analysis, followed by one-way ANOVA Tukey test (two-sided) ($^*P < 0.05$, $^{**}P < 0.01$, $^{***}P < 0.001$, $^{****}P < 0.0001$).

that $d_{33\text{eff}}$ does not increase with vertical polarization field within the measurement conditions. Moreover, second harmonic generation (SHG), a nonlinear optical phenomenon that occurs in non-centrosymmetric structures, is adopted to characterize local piezoelectric responses in PLLA/RS nanofibers (Supplementary Fig. 8). RS crystal particles embedded within the PLLA matrix exhibit significantly stronger SHG signals than the surrounding fibers in the SHG intensity map (Supplementary Fig. 8b), further confirming the contribution of micron-sized RS crystals to the overall piezoelectricity of the nanofibers.

Figure 2f and Supplementary Table 1 compare the measured effective piezoelectric coefficient and the calculated piezoelectric voltage coefficient of PRSC nanofibers with those of representative flexible piezoelectric materials reported in the literature^{42,43,47,49,59–65}. The g_{33} value of PRSC (1909.2 mV m N⁻¹), indicating voltage-generating capability, is obtained using the method described in Supplementary Table 1, based on a measured relative permittivity (ϵ_r) of 2.32 ± 0.19 . The results demonstrate that PRSC nanofibers exhibit excellent piezoelectric performance, with a $d_{33\text{eff}}$ exceeding those of previously reported biodegradable and flexible materials as well as PVDF, and a g_{33} much greater than both biodegradable and non-degradable counterparts, while retaining excellent flexibility. These features highlight their potential for a broad range of bioelectronic applications involving interfaces with soft biological tissues.

Piezoelectric materials that convert US-induced mechanical stimuli into electrical signals hold significant potential for the wireless delivery of electrical stimulation in deep tissues. To evaluate the US piezoelectric response of PRSC films, a programmable US probe (DYM-1M, 1 MHz center frequency, Supplementary Fig. 9a, left) and a clinical US therapy device (Haifu Echo, Supplementary Fig. 9a, right) are employed. Hydrophone measurements (Supplementary Fig. 9b–d) reveal that DYM-1M probe generates acoustic pressures ranging from 0.23 to 0.8 MPa at a 25 mm distance in DI water, with attenuation through 5 mm of pork tissue ranging from 13.1% to 54.2% depending on the input voltage. The clinical US device (Haifu Echo) produces -1.1 MPa at 1 W cm^{-2} and 50% duty cycle, with 12.7% attenuation through the same pork tissue. Moreover, we fabricate PRSC devices in both film and conduit formats, with the latter designed to mimic nerve structures, and investigate their responses to US stimulation (Fig. 2g). Finite element analysis (FEA) simulations are conducted to assess the average potential difference between the external and internal surfaces of the conduit device, and between the upper and lower surfaces of the film device, serving as indicators of output voltage. The internal surface of the conduit and the lower surface of the film are set to 0 potential. Under identical US stimulation along the z-axis (1 MHz, 1 W cm^{-2}), the average potential difference generated in the conduit device is estimated to be approximately 66.2% of that in the film device (Fig. 2h). Experimental measurement demonstrates that the film and conduit samples generate peak-to-peak voltages (Vpp) of 49 mV and 43 mV (20 V input), respectively, with signal delays of -17 μs , corresponding to

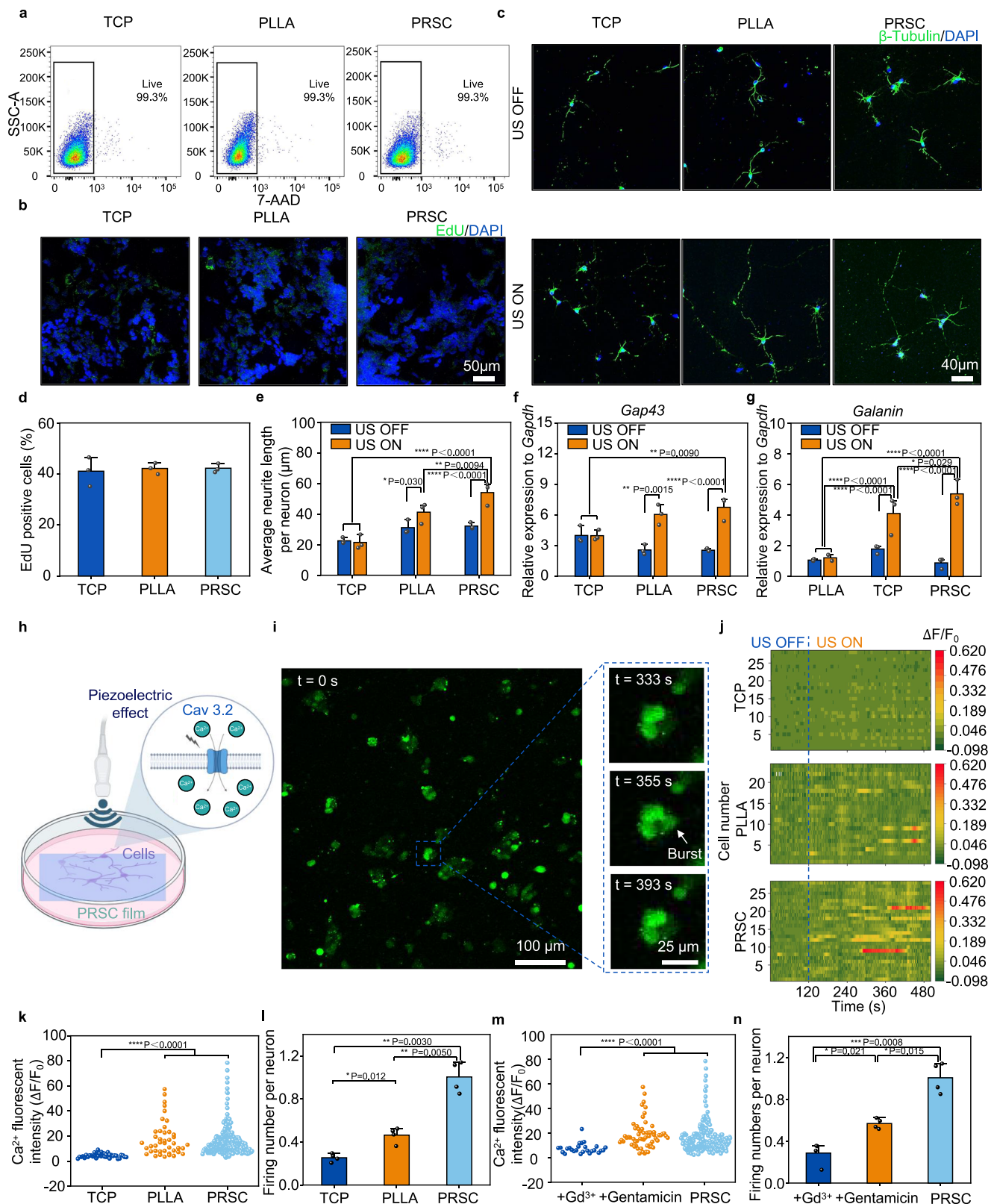
the expected ultrasonic propagation time ($1480 \text{ m s}^{-1} \times 25 \text{ mm} = 16.9 \mu\text{s}$), thereby precluding interference from artifact signals (Fig. 2i).

The output of the conduit devices made of PRSC reaches stability at the 20th US cycle (Supplementary Fig. 10a–b), and increases with input voltage (reaching -130 mV Vpp at 55 V input) (Fig. 2j). In contrast, conduit devices made of PLLA nanofibers only yield output voltage < 10 mV (Supplementary Fig. 10c). Moreover, the PRSC conduit device exhibits desirable angle-insensitive output under US stimulation (Fig. 2k, l). In contrast to the film sample, whose output declines rapidly with increasing incidence angles, the conduit device retains approximately 40.5% of its Vpp even at 90 °, demonstrating greater tolerance to US misalignment. These findings are consistent with previous reports that conduit structures reduce sensitivity to rotational misalignment⁶⁶. These results suggest that, despite a slight reduction in output voltage under US activation, the conduit-shaped device can still effectively deliver the electrical field while accommodating misalignment. Additionally, the output of PRSC conduit devices decreases with increasing thickness of blocking pork tissue (5, 12, and 17 mm) at 0° deflection angle, showing an overall attenuation of -54.2% when blocked by 17 mm tissue (Supplementary Fig. 10d–f). Improved output can be achieved with greater US input power for applications targeting deeper tissues.

US-driven, PRSC-mediated piezoelectric effects on in vitro cells

The biocompatibility of PRSC nanofibers is first evaluated through 7-AAD-based viable cell analysis with flow cytometry (Fig. 3a) and EdU labeling (Fig. 3b) using SH-SY5Y cells, a human neuroblastoma cell line with neuronal characteristics widely used for reproducible electrophysiological assessments of piezoelectric responsiveness^{67,68}. The viability of cells cultured on tissue culture polystyrene (TCP group), PLLA nanofibers (PLLA group) and PRSC nanofibers (PRSC group) exceeds 99.3%, indicating no apparent adverse effects of PRSC (Fig. 3a). EdU staining is used to evaluate cell proliferation (Fig. 3b) and the EdU-positive cell percentages of all groups are shown in Fig. 3d. The percentage of EdU-positive cells in the PRSC group was $42.1 \pm 1.0\%$, which was comparable to that of the TCP group ($43.2 \pm 1.2\%$) and the PLLA group ($41.6 \pm 1.2\%$) with no significant differences. Such results suggest that PRSC does not exert an inhibitory effect on cell proliferation. Based on the above results and analysis, we believe that PRSC does not interfere with the cell proliferation process.

As electrical stimulation has been reported to facilitate axon elongation both in vivo and in vitro^{69–71}, we investigate the impact of electrical stimulation generated by PRSC under US stimulation on the growth behavior of neurons. Primary rat spinal cord neurons, sharing similar molecular phenotypes and ion channel expression with dorsal root ganglia (DRG) neurons, are employed to evaluate axonal elongation. US is applied using the Haifu Echo device, 2 mins per day, with 1 MHz, 1 W cm^{-2} and 50% duty cycle. After three days of culture with (US ON group) or without (US OFF group) US activation, immunofluorescence imaging of spinal cord neurons is performed (Fig. 3c) and



the corresponding statistical results of average neurite length is given in Fig. 3e. US applied to TCP shows no significant effect on axonal growth. In contrast, PRSC combined with US significantly enhances neurite growth compared with the PRSC US OFF group ($P < 0.0001$), and both the TCP US ON group ($P < 0.0001$) and the PLLA US ON group ($P = 0.0094$). Furthermore, the expression of neurite growth-related genes is analyzed using quantitative reverse transcription polymerase

chain reaction (RT-qPCR) (Fig. 3f, g). *Gap43* is closely associated with axonal growth, synaptic plasticity, and neuronal differentiation, making it an important indicator for evaluating neural remodeling and repair processes^{72,73}. *Galanin* is involved in various physiological and pathological functions, including regulation of neurotransmission, neuroprotection, and modulation of the immune response in the nervous system⁷⁴. Relative expression levels of *Gap43* and *Galanin* to

Fig. 3 | Biocompatibility and in vitro modulation of cell activities through US-driven piezoelectric effects of PRSC films. **a** Representative flow cytometry plots of SH-SY5Y cells stained with 7-AAD seeded on the tissue culture plastics (TCP), PLLA nanofibers and PRSC nanofibers. **b** Representative images of SH-SY5Y cells seeded on TCP, PLLA and PRSC for 3 days. EdU: green, DAPI: blue. **c** Representative fluorescent images of rat primary spinal cord neurons seeded on TCP, PLLA, and PRSC for 3 days, with or without US stimulation (1MHz, 1.1 Mpa, 2 min per day). DAPI: blue and β -Tubulin: green. **d** Statistical results of EdU positive cells in the TCP, PLLA and PRSC groups. **e** Statistical results of the average neurite length per neuron in the TCP, PLLA and PRSC groups. **f**, Relative expression of *Gap43* to *Gapdh* in rat primary spinal cord neurons. **g** Relative expression of *Galanin* to *Gapdh* in rat primary spinal cord neurons. **h** Schematic illustration of the activation of calcium activities of cells through US-driven piezoelectric effects of PRSC films. **i** Calcium images of the SY5Y-SH cells in the PRSC group (calcium, green). Left: Photo of SY5Y-SH cells following the loading of calcium dye at 0 s. Right: Time-series images of

calcium dynamics within the cell. **j** Representative calcium signal traces of SY5Y-SH cells of the TCP, PLLA, and PRSC groups. US stimulation is initiated at 120 s (blue dash line) and continues until 480 s. **k** Statistical results of the Ca^{2+} fluorescent intensity of every firing between 300 s to 480 s under US stimulation of the TCP, PLLA and PRSC groups. **l** Statistical results of the firing number per neuron between 300 s to 480 s of the TCP, PLLA and PRSC groups. **m** Statistical results of the Ca^{2+} fluorescent intensity of every firing between 300 s to 480 s under US stimulation of the PRSC group, and PRSC loaded with Gd^{3+} and Gentamicin, respectively. **n** Statistical results of the firing number per neuron between 300 s to 480 s of the PRSC group, and PRSC loaded with Gd^{3+} and Gentamicin, respectively. In **d–g**, **l** and **n**, data are shown as mean \pm s.d. In **d–g**, $n = 3$ independent experiments. In **l** and **n**, $n = 4$ independent experiments. The SPSS software package (version 26.0) is used for the statistical analysis, followed by one-way ANOVA Tukey test (two-sided) ($P < 0.05$, $^{*}P < 0.01$, $^{***}P < 0.001$, $^{****}P < 0.0001$). Panels **h** is created in BioRender. Sheng, X. (2025) <https://BioRender.com/rzyvjlp>.

Gapdh remain similar without US exposure in all the groups, while a significant increase in gene expression is observed in PLLA and PRSC groups following US treatment (Fig. 3f, g). These findings indicate that PRSC can effectively introduce electrical cues into the biological environment during US activation, promoting axonal elongation and enhancing the expression of growth-related genes, thereby benefiting nerve repair.

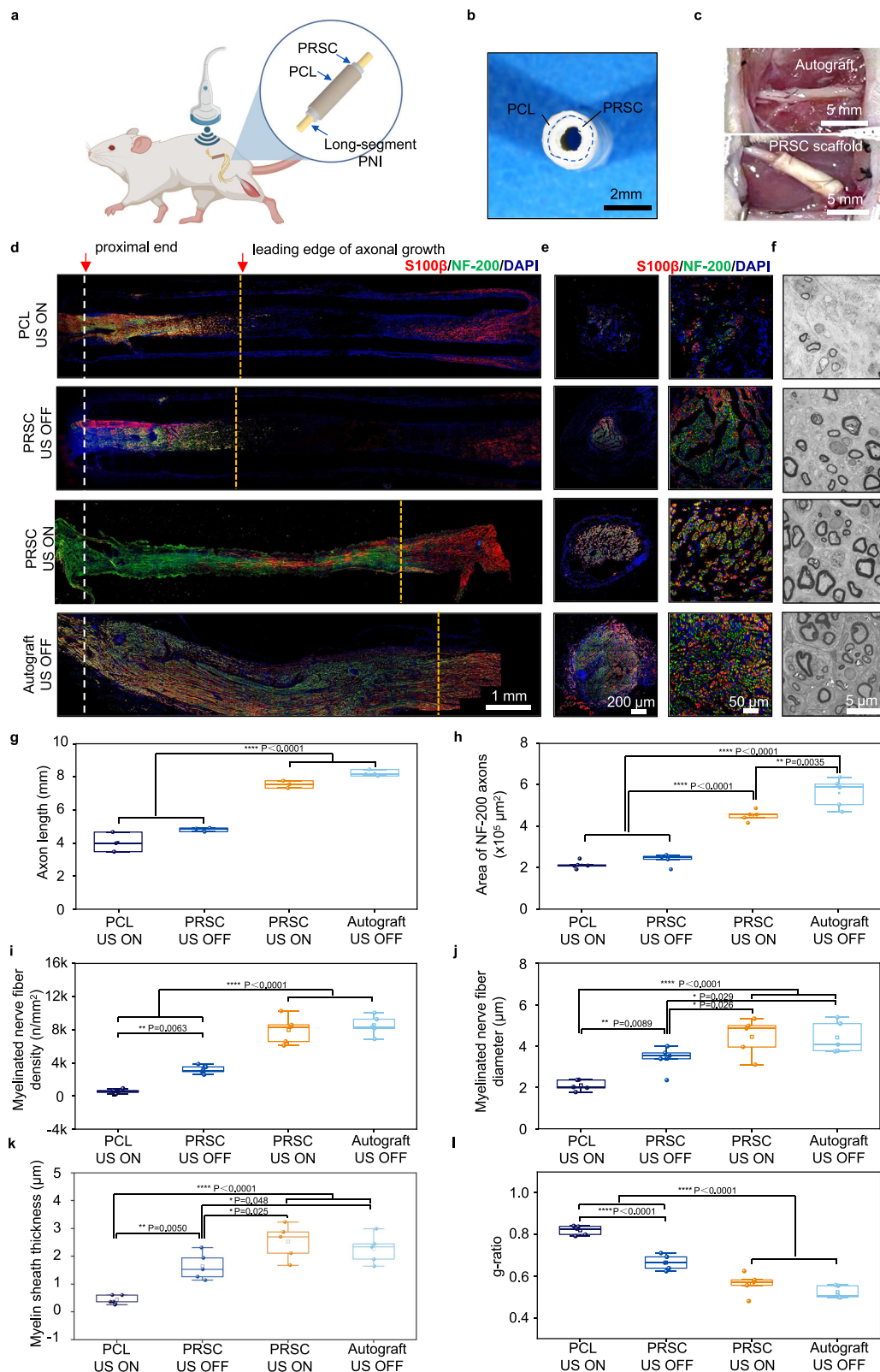
Electrical stimulation has been shown to modulate intracellular calcium flux via voltage-gated calcium channels (VGCCs, such as Cav 3.2), which act as key transducers of guidance cues by regulating actin dynamics, microtubule organization, and regeneration-related proteins to influence neuronal growth^{75–78}. Calcium dynamics in SH-SY5Y cells cultured on PRSC nanofibers under US stimulation are therefore investigated using Fluo-4 AM as the indicator (Fig. 3h). Figure 3i shows a representative calcium image at 0 s in the PRSC group, along with a time-series of fluorescence images capturing intracellular calcium influx in a single cell under US stimulation (starts at 120 s, 1MHz, 1W cm^{-2} , 50% duty cycle) (supplementary Movie 1). To quantify calcium activity, changes in fluorescence intensity ($\Delta F/F_0$) are measured for each neuron over a 500 s period (Fig. 3j). Significantly greater increases in fluorescence intensity are detected in the PRSC and PLLA groups compared with the TCP group ($P < 0.0001$) (Fig. 3k). The number of calcium transients (firing events) per neuron during US stimulation (120–480 s) is also quantified (Fig. 3l). The frequency of calcium activity in the PRSC group is significantly higher than that in the PLLA ($P = 0.0050$) and TCP ($P = 0.0030$) groups. These results suggest that the US-driven, PRSC-mediated piezoelectric stimulation effectively enhances calcium dynamics in SH-SY5Y cells. To further investigate the underlying mechanism, selective channel inhibitors are applied to assess their effects on calcium activity in the presence of PRSC under US stimulation. Selective inhibition of the Cav3.2 channel with gadolinium ions (Gd^{3+}) leads to a marked reduction in $\Delta F/F_0$ and firing numbers (Fig. 3m, n). In contrast, treatment with gentamicin, an inhibitor of mechanosensitive channels, does not significantly alter $\Delta F/F_0$ compared with the PRSC group ($P > 0.05$), while the firing number is reduced ($P = 0.015$), yet remains higher than that in the Gd^{3+} group ($P = 0.021$). Together, these results indicate that the enhanced calcium influx in SH-SY5Y cells is primarily attributed to the US-driven PRSC-mediated piezoelectric effects rather than the US-induced mechanical vibration. Further analysis of calcium dynamics in the PRSC group over different time intervals (Supplementary Fig. 11) reveals that the number of calcium transients during the second interval (300–480 s) is significantly higher than during the first interval (120–300 s), suggesting an incubation period required for calcium channel activation.

Biodegradable piezoelectric scaffold devices for nerve regeneration

We explore whether the US-driven piezoelectric effects induced by PRSC can facilitate the recovery of damaged tissues. Electrical

stimulation presents a robust, non-pharmacological approach to promote nerve regeneration⁷⁹. However, the development of miniaturized, biodegradable devices capable of delivering wireless, continuous stimulation beyond the surgical window remains a significant challenge for maximizing therapeutic efficacy. To evaluate the regenerative potential of PRSC, a piezoelectric scaffold device is developed to deliver electrical stimulation under US activation for the repair of long-segment (10 mm) sciatic nerve injury (Fig. 4a). The device consists of an inner conduit composed of PRSC nanofibers, while the outer non-aligned polycaprolactone (PCL) layer provides structural support (Fig. 4b). The inner PRSC layer is unencapsulated to enable effective delivery of electrical cues under ultrasound activation. We evaluate the US-mediated electrical output of the PRSC/PCL scaffold device in 1 wt% agarose hydrogel to simulate the in vivo environment. The results show that the scaffold can generate voltage output for up to 14 days, retaining over 45% of its initial output during the first 7 days (Supplementary Fig. 12). This operational timeframe is extended compared with unencapsulated PRSC films in DI water (Supplementary Fig. 5f), likely due to protection by the external PCL layer and the lower volume of surrounding fluid. The piezoelectric scaffold is expected to generate electric fields of -10 – 70 mV mm^{-1} under US activation, within the effective range for promoting nerve regeneration^{79,80}, and can be further enhanced by increasing the US input. Overall, the sustained electrical cues generated by the piezoelectric scaffold device under US stimulation during the early phase of nerve injury are expected to trigger regenerative cascades and support long-term recovery of damaged nerve tissue^{79,81,82}. The piezoelectric scaffold is implanted at the injury site (Fig. 4c), and therapeutic outcomes are evaluated with and without US activation (PRSC US ON and PRSC US OFF), alongside comparisons to PCL scaffolds (PCL US ON) and the autograft group (Autograft US OFF) which represents standard treatment. PCL scaffolds without US activation (PCL US OFF), and PLLA/PCL scaffolds with and without US activation (PLLA US ON and PLLA US OFF) are also included as reference groups. US stimulation is administered for 20 min daily at a fixed time over 14 consecutive days post-injury using the Haifu Echo device. The stimulation parameters are set as follows: frequency of 1 MHz, intensity of 1 W cm^{-2} , duty cycle of 50%.

Immunofluorescence images of longitudinal sections of regenerated nerve tissue at 4 weeks postimplantation are shown in Fig. 4d and Supplementary Fig. 13, with white and yellow dotted lines indicating the proximal end and leading edge of the regenerating axons, respectively. Quantitative analysis reveals that axon length in the PRSC US ON group (7.53 ± 0.18 mm) is comparable to that in the Autograft US OFF group (8.20 ± 0.17 mm), and significantly greater than in the other groups (Fig. 4g and Supplementary Fig. 13b). Cross-sectional immunofluorescent images of regenerated nerve segments (midpoint, 5 mm from the proximal end) at 12 weeks postimplantation show that the axonal area in the PRSC US ON group is smaller than that in the



Autograft US OFF group, but significantly larger than in the other groups (Fig. 4e, h and Supplementary Fig. 14).

To evaluate myelination in regenerated nerves, toluidine blue staining (Supplementary Fig. 15a) is performed on distal nerve sections at 12 weeks postimplantation. The PRSC US ON and Autograft groups exhibit significantly higher densities of myelinated nerve fibers compared to other groups (Fig. 4i and Supplementary Fig. 15b).

Transmission electron microscopy (TEM) is used to assess the ultrastructure of myelin sheaths and regenerated axons, providing insights into remyelination maturity (Fig. 4f and Supplementary Fig. 15a). The PRSC US ON group shows comparable myelinated fiber diameter, myelin sheath thickness, and g-ratio to the Autograft group, and significantly greater values relative to other groups (Fig. 4j–l, Supplementary Fig. 15c–e), indicating enhanced remyelination. Myelination is

Fig. 4 | PRSC promotes sciatic nerve regeneration under ultrasound stimulation. **a** Schematic illustration of the biodegradable piezoelectric scaffolds (PRSC) consisting of an inner layer of PRSC and an outer layer of non-aligned PCL for US-mediated long-segment peripheral nerve regeneration. **b** Optical image of the biodegradable PRSC scaffold. **c** Optical images of autograft and PRSC implantation. **d** Immunofluorescent images of the longitudinal sections of regenerated nerve segments at 4 weeks postimplantation of the PCL US ON, PRSC US ON, PRSC US OFF and Autograft US OFF groups. Immunohistochemical staining: axons (NF200, green), Schwann cells (S100 β , red), and nuclei (DAPI, blue). **e** Immunofluorescent images of the cross-section of regenerated nerves at the middle of the nerve segments (5 mm from the proximal end) at 12 weeks postimplantation. Immunohistochemical staining: axons (NF200, green), Schwann cells (S100 β , red), and nuclei (DAPI, blue). **f** TEM images of the cross-section of regenerated nerve segments at the distal end at 12 weeks postimplantation. **g** Statistical results of the length of regenerated axons at week 4. **h** Statistical results of axonal area of the cross-section

of the regenerated nerve segment at the midpoint at 12 weeks postimplantation. **i** Statistical results of myelinated nerve fiber density of regenerated at the distal end at 12 weeks postimplantation. **j** Statistical results of the average diameter of myelinated nerve fiber at the distal end at 12 weeks postimplantation. **k** Statistical results of the average thickness of myelin sheath at the distal end at 12 weeks postimplantation. **l** Statistical results of average g-ratio at the distal end at 12 weeks postimplantation. In **g–l**, The box plot presents the median (center line), lower quartile (lower border), upper quartile (upper border), maximum (upper whisker) and minimum (lower whisker), which are ≤ 1.5 times the interquartile range. In **d** and **g**, $n = 3$ independent experiments. In **e**, **f**, and **h–l**, $n = 5$ independent experiments. The SPSS software package (version 26.0) is used for the statistical analysis, followed by one-way ANOVA Tukey test (two-sided) ($P < 0.05$, $^{**}P < 0.01$, $^{***}P < 0.001$, $^{****}P < 0.0001$). Part of panels **a** is created in created in BioRender. Sheng, X. (2025) <https://BioRender.com/kwzrucv>.

analyzed at the distal end of the nerve defect (1 mm from the scaffold-host interface), a region that directly reflects the quality of newly formed nerve fibers that have grown through the scaffold and connected to the distal host nerve. Collectively, these findings demonstrate that the piezoelectric PRSC scaffold, when activated by US, effectively promotes nerve regeneration, outperforming PCL or PCL/PLLA scaffolds with weaker piezoelectric properties.

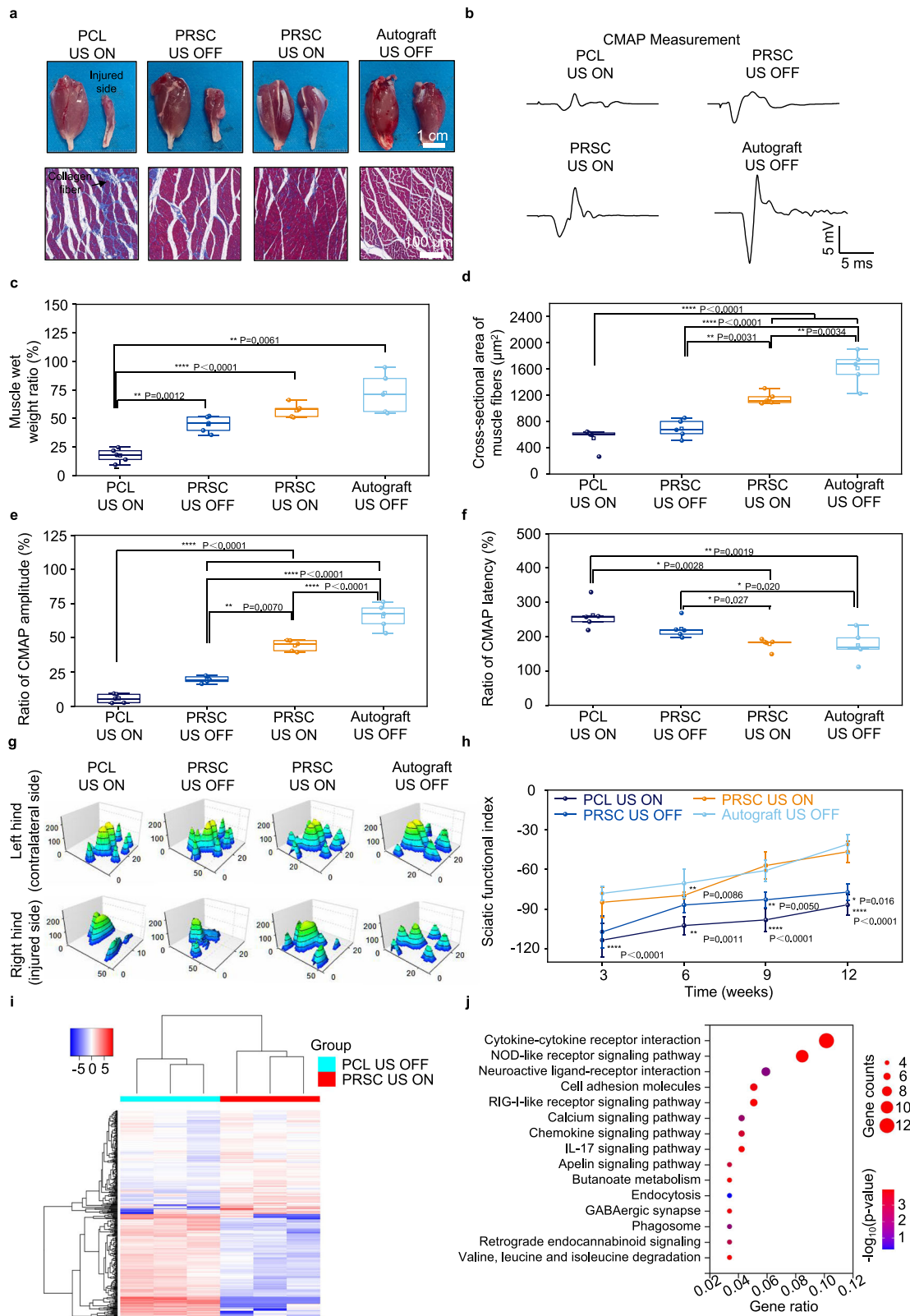
Sciatic nerve injury often results in muscle atrophy and impaired motor function. To assess functional recovery, gastrocnemius muscle evaluation, electrophysiological analysis, and walking track assessments are performed. Muscle atrophy is evaluated by measuring wet weight and conducting Masson's trichrome staining at 12 weeks postimplantation. Representative gross images of the gastrocnemius muscle are shown in Fig. 5a and Supplementary Fig. 16a, with the injured side on the right and the contralateral side on the left. The wet weight ratios (operative side vs. control side) of the PRSC US ON and Autograft groups are significantly higher than those of the other groups (Fig. 5c and Supplementary Fig. 16c). Masson's trichrome staining reveals the distribution of collagen fibers and muscle tissue (Fig. 5a and Supplementary Fig. 16a). The average cross-sectional areas of muscle fibers in the PRSC US ON group ($1155 \pm 93 \mu\text{m}^2$) are smaller than the Autograft group ($1612 \pm 257 \mu\text{m}^2$) but significantly larger than in the other groups, indicating reduced collagen deposition and less muscle atrophy (Fig. 5d and Supplementary Fig. 16d).

Electrophysiological studies assess nerve conduction recovery by measuring compound motor action potential (CMAP) in the target gastrocnemius muscle following electrical stimulation (1.5 mA, 0.1 ms) of the proximal stump of the injured sciatic nerve. Representative CMAP curves for each group are shown in Fig. 5b and Supplementary Fig. 16b. Ratios of CMAP amplitude and latency (injured side vs. contralateral side) are analyzed (Fig. 5e, f and Supplementary Fig. 16e, f). While latency ratios differ minimally across groups, the PRSC US ON group shows a CMAP amplitude ratio lower than that of the Autograft group but significantly higher than those of the other groups, indicating that the US-driven PRSC scaffold promotes nerve reinnervation and mitigates nerve atrophy.

The CatWalk system is used to assess the walking track every three weeks postoperatively to monitor motor function recovery. Representative 3D plantar pressure distribution maps of the affected and contralateral sides are shown in Fig. 5g and Supplementary Fig. 17a. The x and y axes represent the length and width of footprints, while the z axis indicates relative plantar pressure. The results show that the print area and plantar pressure in the PRSC US ON group are comparable to those in the autograft group. The sciatic function index (SFI), calculated from four distinct footprint parameters, serves as a metric for sciatic nerve function recovery. SFI values closer to 0 reflect better motor recovery, while values near -100 indicate severe impairment. Statistical analysis shows that SFI values reach their lowest point at week 3 in all groups and gradually improve over time. By

weeks 9 and 12, the SFI of the PRSC US ON group shows no significant difference from the autograft group, and is significantly higher than in the other groups (Fig. 5h and Supplementary Fig. 17b). Furthermore, H&E staining at 12 weeks postimplantation shows no significant inflammation with PRSC implantation (Supplementary Fig. 18). These findings suggest that the PRSC nerve scaffold, under US stimulation, effectively promotes motor function recovery.

To elucidate the mechanisms by which the PRSC-mediated, US-driven piezoelectric effect promotes peripheral nerve regeneration, we perform transcriptomic sequencing of regenerated tissues at 3 weeks postimplantation. We compare gene expression profiles between the PRSC US ON and PCL US OFF groups. Differential expression analysis reveals 176 upregulated and 180 downregulated genes in the PRSC US ON group relative to the PCL US OFF group (Fig. 5i, Supplementary Fig. 19a). To interpret the functional implications of these gene expression changes, we conduct gene enrichment analyses using the Kyoto Encyclopedia of Genes and Genomes (KEGG, Fig. 5j) and Gene Ontology (GO, Supplementary Fig. 19b) databases. KEGG analysis indicates that enriched pathways associated with peripheral nerve regeneration span several domains: metabolic pathways (e.g., butanoate and valine metabolism) suggest a neuroregenerative metabolic shift^{83–85}; cytokine and immune-related pathways (e.g., “cytokine-cytokine receptor interaction” and “NOD-like receptor signaling”) implicate inflammation modulation; neurotransmitter-related pathways (e.g., “GABAergic synapse”) may contribute to a pro-regenerative microenvironment; and calcium signaling can enhance regeneration-associated proteins. GO terms such as “astrocyte projection” reflect neurophysiological adaptations, while “GTP binding” and related categories suggest roles in intracellular signaling and immune microenvironment regulation. Gene set enrichment analysis (GSEA; Supplementary Fig. 19c–e) further highlights the activation of pathways, including “RIG-I-like receptor signaling”⁸⁶ and those related to amino acid and fatty acid metabolism. Notably, fatty acid oxidation pathways are known to support phagocytic activity and energy production, both of which are critical during early stages of nerve regeneration⁸⁷. As the effects of electric cues on nerve repair are reported to be closely related to calcium dynamics, we further analyze related genes of calcium signaling pathways and regulation of neuronal excitability. The results reveal an increase in *Adrb1*, a Gs-coupled receptor that modulate calcium signals, which could activate the cAMP-protein kinase A (PKA) signaling axis to initiate transcriptional programs that underpin axonal growth^{88,89} (Supplementary Fig. 19f). Moreover, calcium influx directly drives bidirectional regulation of synaptic transmission through retrograde endocannabinoid signaling pathway and other transmission pathway: down-regulation of *Gria3* (AMPA receptor GluA3 subunit) inhibits glutamatergic excitatory transmission, while reduces *Slc12a5* (KCC2 potassium-chloride cotransporter) limits GABAergic inhibitory effect, modulating excitation-inhibition balance through *Gabrr1* (GABA- $\rho 1$ receptor) and



Abat (GABA transaminase)⁹⁰ (Supplementary Fig. 19g). The modulated neuronal excitability could have positive effects to promote regeneration⁹¹. These preliminary transcriptome analyses provide evidence that ultrasound-mediated piezoelectric stimulation promotes nerve repair. Nevertheless, further in-depth validation of the transcriptome screening results could reveal detailed underlying mechanisms and help guide therapeutic interventions.

Biodegradable piezoelectric strain sensors for intestinal motility monitoring

Next, we aim to investigate the strain-sensing functionality of PRSC. Acute mesenteric ischemia (AMI) is a life-threatening condition caused by the sudden disruption of intestinal blood flow, leading to ischemia and inflammation⁹². Early diagnosis is critical to improve prognosis and reduce mortality⁹³⁻⁹⁵. However, current diagnostic tools, including

Fig. 5 | PRSC promotes motor function recovery of injured sciatic nerves at 12 weeks postimplantation under ultrasound stimulation. **a** Representative gross images of the isolated gastrocnemius muscles of the injured side (right) and the contralateral side (left), and corresponding masson's trichrome staining images of the cross section of gastrocnemius muscles of the injured side. **b** Representative signal traces of compound motor action potential (CMAP) at the injured side. Electrical stimulation: 1.5 mA, 0.1 ms. **c** The wet weight ratio (injured side/contralateral side) the gastrocnemius muscle. **d** Cross-sectional area of muscle fibers at the injured side. **e** Statistical results of CMAP amplitude ratio (injured side/contralateral side). **f** Statistical results of CMAP latency ratio (injured side/contralateral side). **g** Representative 3D plantar pressure distribution of the walking track of SD

rats at 12 weeks postoperatively. **h** Sciatic functional index of SD rats at 3, 6, 9, and 12 weeks postoperatively. Statistical significance is analyzed with respect to the PRSC US ON group. **i** Heatmap listing significantly changed genes in the PRSC US ON group compared to the control group (PCL US OFF group). **j** KEGG pathway enrichment analysis of the differentially expressed genes. In **c–f**, The box plot presents the median (center line), lower quartile (lower border), upper quartile (upper border), maximum (upper whisker) and minimum (lower whisker), which are ≤ 1.5 times the interquartile range. In **h**, data are shown as mean \pm s.d. In **a–h**, $n = 5$ independent experiments. The SPSS software package (version 26.0) is used for the statistical analysis, followed by one-way ANOVA Tukey test (two-sided) ($P < 0.05$, $^{*}P < 0.01$, $^{**}P < 0.001$, $^{***}P < 0.0001$).

laboratory tests and imaging technologies, lack sensitivity and timeliness⁹³. Here, we present a flexible, biodegradable strain sensor based on PRSC, integrated with a wireless circuit for real-time monitoring of colonic peristalsis. This platform offers a promising approach for the early detection of intestinal dysfunction.

The structure of the biodegradable piezoelectric strain sensor is illustrated in Fig. 6a. The sensor features a PRSC-based sensing layer sandwiched between biodegradable molybdenum (Mo, 10 μm) electrodes. Device patterning is achieved via femtosecond laser ablation, enabling three sensing channels for synchronous monitoring. To reduce water penetration and extend the operational time frame, the sensor is encapsulated between two layers of flexible, biodegradable PLCL ($\sim 100 \mu\text{m}$). The detailed fabrication process is shown in Supplementary Fig. 20a. The device demonstrates excellent flexibility (Supplementary Fig. 20b) and undergoes gradual degradation in PBS at 65 $^{\circ}\text{C}$ (Supplementary Fig. 20c). The polymer components hydrolyze and disintegrate by day 21, while the Mo electrodes are expected to dissolve over a longer period. The longitudinal pressure-voltage response of the strain sensor is evaluated via impact testing, as shown in Fig. 6b. All three channels exhibit similar responses, with an average sensitivity of $0.049 \pm 0.003 \text{ V kPa}^{-1}$ in the 0–40 kPa range, demonstrating consistent pressure-sensing performance. Voltage output under bending strain is also assessed to simulate intestinal contractions. Results show a linear increase in open-circuit voltage with increasing bending deformation ($R^2 > 0.99$) (Fig. 6c and Supplementary Fig. 21), indicating the feasibility of monitoring colonic motility.

To assess in vivo monitoring performance, the biodegradable piezoelectric strain sensor is affixed to the outer surface of the colon in New Zealand white rabbits using a biodegradable adhesive hydrogel previously developed by our group⁹⁶ (Fig. 6d). The sensor forms conformal contact with the colon wall, enabling the detection of intestinal contractions. A flexible printed circuit board (FPCB) connects the sensor to a wireless transmission module for real-time, untethered data acquisition (Supplementary Fig. 22a). Measured signals acquired via the wireless transmission module exhibit excellent agreement with the test input signals, as shown in Supplementary Fig. 22b, thereby validating the recording fidelity of the wireless system. Intestinal motility is recorded under normal conditions, following pharmacological intervention, and during AMI.

Representative data segments from different stages are extracted and analyzed. Figure 6e presents the recorded signals from one channel during the initial stage of colonic motility under normal conditions in three rabbits. The signals are first processed with a 10 Hz low-pass filter and analyzed using Empirical Mode Decomposition (EMD) to isolate peristalsis-related components and remove physiological artifacts such as respiration and cardiac rhythms. EMD decomposes the signal into a set of Intrinsic Mode Functions (IMFs), each associated with distinct frequencies determined via short-time Fourier transform (STFT), implying different physiological behavior⁹⁷. For example, in a representative recording under normal conditions (Supplementary Fig. 23), IMF4 corresponds to a primary frequency range of

0.23–0.33 Hz (14–20 contractions per minute), aligning with the spontaneous colonic rhythmic contractions observed experimentally. IMF6, at approximately 0.04 Hz (~ 2 contractions per minute), aligns with reported frequencies characteristic of giant migrating contractions (GMCs)^{98–100}. In addition, IMF1 corresponds to power frequency noise (~ 50 Hz). IMF2 may be related to the rabbit's respiration and heartbeat (1–2 Hz), while IMF3 (~ 0.3 –1 Hz) and IMF5 (0.05–0.2 Hz) exhibit broader frequency distributions. This analysis facilitates the identification and extraction of meaningful colonic motility signals from complex biological data. The IMF (i.e., IMF4 under normal conditions) that aligns with the frequency of intestinal peristalsis, is therefore selected for subsequent assessment.

The amplitude, frequency, and propagation wave velocity can therefore be analyzed to interrogate the intestinal health status. The intensity of spontaneous rhythmic colonic contractions can be quantified by the Vpp. Figure 6f presents the statistical analysis of Vpp values across all monitored channels at different stages under normal conditions, showing that Vpp remains consistently within the range of 0–9 mV. Moreover, as the strain sensor channels are spatially distributed along the colon, peristaltic wave velocity can be estimated by calculating the phase delay between each two channels (Supplementary Fig. 24). Figure 6g shows the statistical analysis of wave velocities at various stages under normal intestinal conditions, revealing stable motility over time. Wave velocities calculated based on different channel pairs yield comparable results. In addition, time-frequency maps corresponding to spontaneous rhythmic contractions further illustrate the frequency distribution of contractions. Representative results confirm a consistent peristaltic state at different stages (Fig. 6h and Supplementary Fig. 25).

Peristalsis monitoring under pharmacological intervention is conducted using domperidone, a peripheral dopamine D2 receptor antagonist known to enhance gastrointestinal motility (Fig. 6i). Peristaltic signals are recorded from the colon surface 1 h after oral administration of domperidone (0.5 g kg^{-1}), with representative IMF traces at different stages shown in Supplementary Fig. 26a–f. Across all channels, the amplitude of spontaneous rhythmic contractions increases post-administration, then gradually declines (Fig. 6j), and the return to baseline levels amplitude by ~ 2 h post-domperidone intervention. Similarly, the propagation velocity of peristaltic waves initially increases and subsequently returns to normal values (Fig. 6k). Time-frequency analysis reveals a broader distribution of contraction frequencies shortly after drug administration, indicating a more intense and complicated peristaltic state that later stabilizes and shifts to lower frequencies (Fig. 6l and Supplementary Fig. 26g–l).

Furthermore, mesenteric ischemia is induced by ligating the mesenteric artery supplying the colonic segment where the sensor is affixed (Fig. 6m). Within 2 h post-ligation, pronounced colonic swelling and a reduction in peristaltic amplitude are observed (Supplementary Fig. 27). The evolution of spontaneous rhythmic contraction amplitude (Vpp) following ischemia is shown in Fig. 6n and Supplementary Fig. 28a–f, revealing an initial transient increase followed by a rapid decline. Consistent trends are observed in peristaltic wave velocity

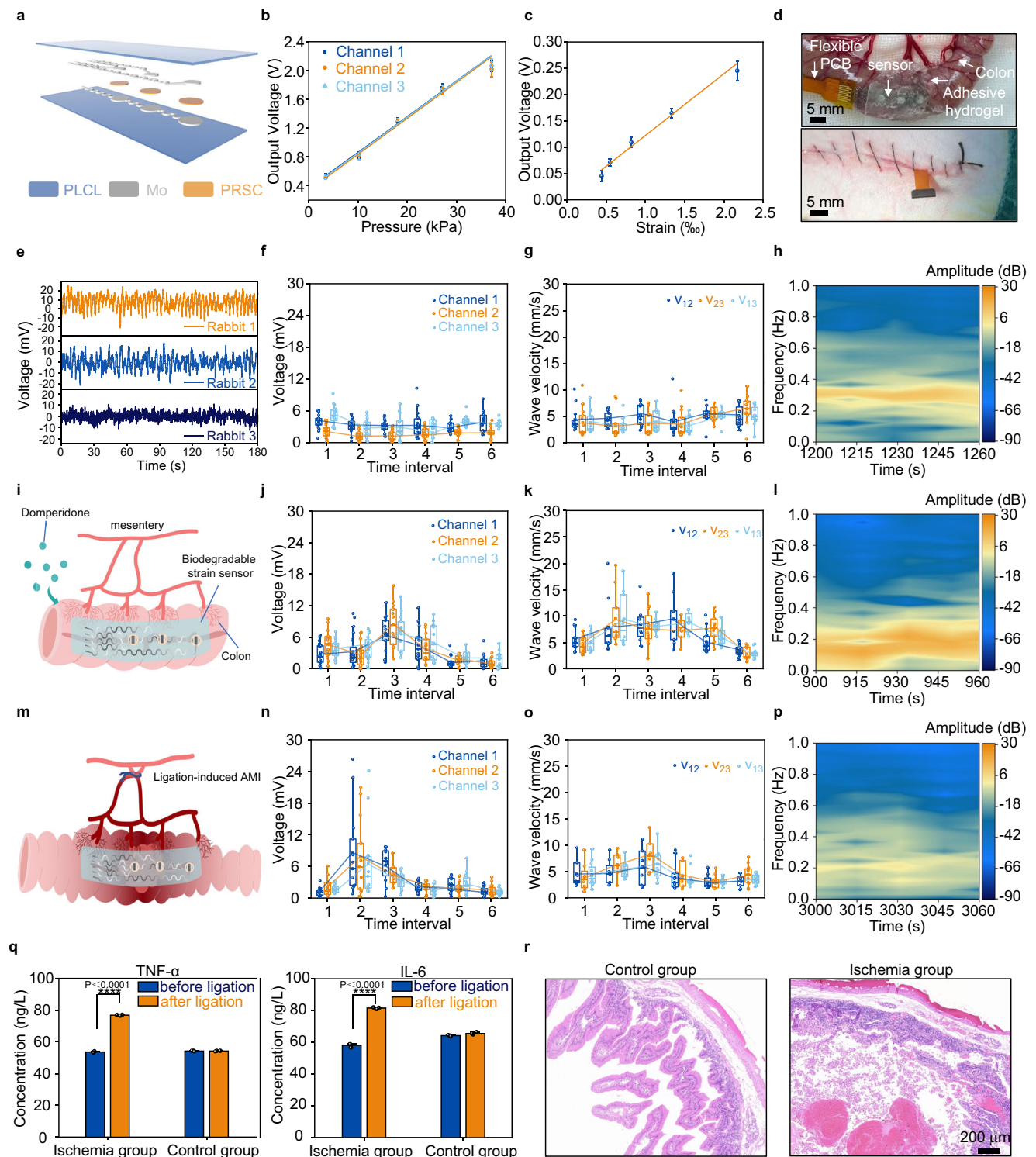


(Fig. 6o) and time-frequency profiles (Fig. 6p and Supplementary Fig. 28g–l). This two-stage response reflects a compensatory increase in motility during the early ischemic phase, likely driven by temporary vascular autoregulation, which is unsustainable over time. As ischemia progresses, peristaltic activity sharply diminishes. These dynamic changes are successfully captured in real time by the piezoelectric strain sensor. The onset of acute mesenteric ischemia is confirmed by elevated inflammatory markers and histological analysis (Fig. 6q, r). Two h after mesenteric artery ligation, the concentrations of TNF- α and IL-6 in the blood of ischemic rabbits increase significantly ($P < 0.0001$), while no significant changes are observed in the sham-

operated control group. H&E staining reveals marked structural disruption and disorganization of colonic tissue in the ischemia group, indicating severe intestinal necrosis. Overall, these measurements demonstrate that the PRSC-based biodegradable piezoelectric strain sensor enables real-time detection of colonic peristalsis, including amplitude, wave velocity, and frequency, supporting timely diagnosis of intestinal dysfunction.

Discussion

In this study, we introduce an effective materials paradigm and processing strategy for high-performance, bioresorbable, and flexible

Fig. 6 | Biodegradable piezoelectric strain sensors based on PRSC for intestinal peristalsis monitoring. **a** Schematic illustration of the piezoelectric strain sensor. **b** Output voltage of the three channels of the sensor as a function of pressure. **c** Representative output voltage of the strain sensor under various degree of bending deformation. **d** Optical images of the implantation of the sensor on the colon surface of New Zealand white rabbits. **e** Representative voltage output of the sensor demonstrating the intestinal motility at the initial stage in three rabbits. **f** Output voltage of all three channels of the sensor in the normal group over different time intervals during continuous monitoring for 30 min. **g** Peristalsis velocity calculated from the phase difference between different channels of the sensor in the normal group over different time interval. **h** Representative time-frequency diagram measured of the normal group. **i** Schematic illustration of promoting colonic motility in New Zealand white rabbits through Domperidone administration. **j** Output voltage of the three channels of the sensor in the Domperidone administration group at multiple time intervals during continuous monitoring for 2 h. **k** Peristalsis wave velocity calculated from the phase difference between the different channels of the sensor in the Domperidone administration

group over different time interval. **l** Time-frequency diagram measured of the Domperidone administration group during the peak of colonic peristalsis. **m** Schematic illustration of ischemia due to mesenteric artery occlusion. **n** Output voltage of the three channels of the sensor in the ischemia group at multiple time intervals during continuous monitoring for 2 h. **o** Peristalsis wave velocity calculated from the phase difference between the different channels of the sensor in the ischemia group over different time interval. **p** Time-frequency diagram measured of the ischemia group during severe ischemia. **q** Analysis of inflammatory factor levels before and after mesenteric ischemia. **r** H&E staining analysis before and after mesenteric ischemia. In **f**, **g**, **j**, **k**, **n** and **o**, The box plot presents the median (center line), lower quartile (lower border), upper quartile (upper border), maximum (upper whisker) and minimum (lower whisker), which are ≤ 1.5 times the inter-quartile range. In **b**, **c** and **q**, data are shown as mean \pm s.d. In **b**, **c**, **e**–**h**, **j**–**l**, **n**–**r**, $n = 3$ independent experiments. The SPSS software package (version 26.0) is used for the statistical analysis, followed by one-way ANOVA Tukey test (two-sided) ($P < 0.05$, $^{*}P < 0.01$, $^{**}P < 0.001$, $^{***}P < 0.0001$).

piezoelectric nanofibers based on RS crystals and PLLA. By combining electrospinning with vertical uniaxial compression, we address the brittleness of RS by leveraging the flexible PLLA framework, simultaneously enhancing piezoelectric performance and preserving flexibility. The improved piezoelectric performance arises from the oriented distribution of RS crystals within the PLLA fibers, and uniaxial compression further promotes in-plane crystal ordering. We achieve a maximum piezoelectric coefficient of 43.1 ± 3.0 pC N $^{-1}$, nearly an order of magnitude enhancement over pure PLLA nanofibers or RS/PLLA composites fabricated via conventional blending methods. An excellent piezoelectric voltage coefficient of 1909.2 mV m N $^{-1}$ is also attained, significantly surpassing those of both biodegradable and non-degradable piezoelectric counterparts. The PRSC film can be effectively activated by the US, producing tunable output depending on the US power, with potential applications in deep-tissue modulation. Moreover, the water solubility of RS is a key feature for its use as a biodegradable piezoelectric material, but it also challenges material stability. By embedding RS microparticles within the PLLA nanofibers, unencapsulated PRSC achieves an operational timeframe of up to 10 days in PBS at 37 °C. Additional encapsulation of PRSC films with a biodegradable PLCL layer further extends the working lifetime.

These RS-based composite films exhibit excellent biocompatibility and can effectively deliver electrical cues under US stimulation, modulating gene expression and calcium dynamics closely associated with cellular behaviors such as neurite growth. They thus provide a robust material platform for constructing versatile piezoelectric devices that interface with soft biological tissues. We demonstrate that biodegradable piezoelectric scaffold devices significantly promote sciatic nerve regeneration and motor function recovery in rodent under US stimulation. The scaffold devices incorporate an additional PCL layer on the PRSC film and form a conduit shape to structurally guide nerve regrowth, while also providing protection for the PRSC layer and extending its operational timeframe. US-mediated piezoelectric stimulation over 14 days is applied and effectively promotes long-gap nerve regeneration, achieving efficacy comparable to the standard autograft technique, while offering the advantages of avoiding donor nerve sacrifice and enabling wireless stimulation. These results are consistent with previous reports showing that electrical stimulation applied during the early stage of nerve injury can significantly enhance subsequent long-term regeneration^{81,82,101}. The underlying mechanism may involve accelerated progression of Wallerian degeneration¹⁰² and elevated calcium activity and subsequent upregulation of regeneration genes^{101,103,104}, which ultimately promote faster axonal growth. Moreover, based on the PRSC film, a biodegradable piezoelectric strain sensor is developed to enable real-time monitoring of colonic peristalsis. When combined with EMD analysis and a wireless module, the sensor allows remote interrogation of

motility status, providing a promising approach for detecting intestinal dysfunctions such as acute ischemia.

Looking forward, the piezoelectric performance of RS-based nanofibers may be further enhanced through strategies that improve dipole alignment, such as multifield-assisted poling and template-guided self-assembly. Tailoring encapsulation approaches could extend device operational lifetimes, broadening the applicability of these materials in implantable systems. Developing biodegradable, conductive, and flexible multi-channel electrical interconnects and/or degradable miniaturized wireless circuits allows fully implantable and biodegradable platforms. Systematic investigation of optimized US stimulation parameters and the underlying mechanisms, supported by in-depth transcriptome analysis and corresponding verification, may inform improved therapeutic strategies for regenerative medicine. Beyond peripheral nerve repair and gastrointestinal monitoring, RS-based piezoelectric devices hold promise for US-mediated deep-tissue biomedical applications, including cardiac pacing, neuromodulation, drug delivery, etc. Collectively, this work establishes a foundational framework for the development of biodegradable bioelectronic systems for therapeutic intervention and physiological interrogation.

Methods

Fabrication of piezoelectric nanofibers

The micron-sized RS crystal powder was prepared by high-energy ball milling. The RS crystal (Shanghai Aladdin Biochemical Co., Ltd., China), zirconium dioxide (ZrO $_2$) milling balls, and ethanol (Beijing Tongguang Chemical Co., Ltd., China) were loaded into a nylon milling jar, where they underwent thorough grinding for 24 h using a planetary ball mill (QM-3SP2, Nanjing Nanda Instrument Co., Ltd., China). The resulting slurry was then dried at room temperature for over 48 h. To prepare the electrospinning precursor solution, the micron-sized RS crystal powder was mixed into a solution composed of anhydrous dichloromethane (DCM, $\geq 99.9\%$, Sigma-Aldrich, USA) and anhydrous N, N-dimethylformamide (DMF, $\geq 99.9\%$, Sigma-Aldrich, USA) in a 4:1 volume ratio. After stirring for 5 min, poly (L-lactic acid) (PLLA, Mw = 350,000, Jinan Daigang Biomaterial Co., Ltd., China) was added to the suspension, which was then stirred vigorously overnight. The electrospinning process was conducted under ambient conditions with a relative humidity of $40\% \pm 10\%$. A 14-gauge needle was used to deliver the polymer solution at a flow rate of 0.08 mL/min. The setup included an aluminum drum collector wrapped with aluminum foil, positioned 10 cm from the needle tip. An electric field of 28 kV was applied. The resulting PLLA/RS composite nanofibers were vacuum-dried for over 24 h at room temperature to ensure complete solvent removal. PLLA/RS nanofibers with different PLLA to RS mass ratios (4:1, 2:1, 1:1, 1:2) and different rotating speeds (400 rpm, 1000 rpm, 2800 rpm) of electrospinning were investigated. To further improve piezoelectric

performance, the PLLA/RS nanofibers were subjected to uniaxial compression. They were placed in a standard mold (diameter of 80 mm) and compressed using a hydraulic press, to achieve PRSC films. The influence of varying compression forces (2 kN, 30 kN, 50 kN, 100 kN) were investigated. Pure electrospun PLLA films were also fabricated as control samples. Finally, all samples were stored in a dry storage cabinet for long-term preservation under low-humidity conditions.

Evaluation of material morphology, structure, mechanical properties and biodegradability

Material surface morphology was investigated using a field-emission scanning electron microscopy (SEM) system (Zeiss, Germany), and energy-dispersive X-ray spectroscopy (EDS) was employed to analyze the composition of the piezoelectric films. ImageJ software (National Institutes of Health, <http://rsb.info.nih.gov/ij>) was utilized for quantitative analysis of alignment and the diameter of nanofibers and RS crystal particles.

The porosity was characterized using a reported density bottle method¹⁰⁵. Specifically, the density bottle was first filled with ethanol (density ρ_e) and weighed (W_1). Subsequently, the electrospun nanofiber sample (weight W_s ; total volume V_s , calculated as the area multiplied by the thickness) was immersed into the bottle. The bottle was then refilled with ethanol and weighed again (W_2). The scaffold volume of the nanofiber film is equal to the volume of displaced ethanol, i.e., $(W_1 - W_2 + W_s)/\rho_e$. The porosity (φ) was thus calculated using the formula:

$$\varphi = 1 - \frac{W_1 - W_2 + W_s}{V_s \times \rho_e} \quad (1)$$

The functional groups and thermal stability of the samples were analyzed using Fourier transform infrared spectroscopy (FTIR) and thermogravimetric analysis system (X70, NETZSCH, Germany), respectively. The thermogravimetric tests were conducted under a nitrogen atmosphere with a heating rate of 10 °C/min from room temperature to 375 °C. Tensile tests were conducted using a universal testing machine (WDW3020, Kexin Co. Ltd., China) at a strain rate of 0.25 min⁻¹, with specimens of size 5 mm × 40 mm. The tensile modulus was calculated from the stress-strain curves ($n=3$). Degradation experiments were performed by immersing the devices (in planar state) in phosphate-buffered saline (PBS) (changed daily) at 60 °C using a water bath. Time-series images were captured at various stages using an optical microscope. X-ray diffraction (XRD) measurements were conducted at room temperature using a Smartlab 3 kW diffractometer (Rigaku Holdings Corporation, Japan) with Cu-K α radiation ($\lambda = 1.5418 \text{ \AA}$) at 40 kV and 40 mA. Diffractograms were recorded from 10° to 40° (2 θ) with a scan speed of 3° min⁻¹. Normalized XRD spectra are obtained using min-max normalization. The patterns were compared to the ICDD powder diffraction file (PDF) database (PDF 29-1046 for Potassium Sodium Tartrate Hydrate) for phase analysis. Pole figure measurements were performed using a Smartlab 9 kW diffractometer (Rigaku Holdings Corporation, Japan) with Cu-K α radiation ($\lambda = 1.5418 \text{ \AA}$) at 40 kV and 150 mA. The figures were acquired with a scan speed of 2° min⁻¹. Two-dimensional (2D) wide-angle X-ray scattering (WAXS) frames were acquired at room temperature using a Ganesha diffractometer (SAXSLab, USA) with Cu-K α radiation ($\lambda = 1.5418 \text{ \AA}$) at 50 kV and 0.6 mA.

Characterization of piezoelectric properties

The effective piezoelectric $d_{33\text{eff}}$ coefficients were measured at room temperature using a quasi-static d_{33} piezometer (ZJ-3A, Beijing Zhongxingyunke Instrument Co., Ltd., China) under a static force of 0.025 N. Each sample was cut into a size of 5 mm × 5 mm for measurement ($n=6$). The inverse piezoelectric effect of the samples was

evaluated at room temperature using a Micro System Analyzer (MAS-100-3DSV-M, polytec, Derman). The samples were cut into 10 mm × 10 mm slices and fixed onto an aluminum block using room-temperature-cured silver paste (SINWE, China). A platinum (Pt) electrode (thickness: 20 nm; diameter: 1 mm) was deposited onto the sample surface via magnetron sputtering. An alternating current (AC) driving electric field and a direct current (DC) bias electric field were applied to the samples through the Pt electrode and the aluminum block. The out-of-plane vibrational amplitude of the samples was measured using laser Doppler interferometry. The inverse piezoelectric coefficient $d_{33\text{eff}}$ was calculated using the relationship $d_{33\text{eff}} = \Delta z/V_{\text{AC}}$, where Δz represents the vibrational amplitude, and V_{AC} represents the applied AC voltage. The second-harmonic generation (SHG) spectrum of the piezoelectric nanofibers was also studied using a customized SHG microscope¹⁰⁶. Glass slides were cut into 1 cm × 1 cm pieces and affixed to electrospinning aluminum foil substrates using double-sided adhesive tape during electrospinning, with the process duration controlled within 2–3 min to deposit an ultrathin fiber layer. Post-spinning, the fiber-coated slides were carefully removed and subjected to the SHG microscopic analysis.

To test piezoelectric properties under an impact system, the samples ($n=5$) were cut into 15 mm × 15 mm films and sandwiched between aluminum (Al) electrodes. Polyimide tape (3 M5413 HD, 3M, USA) was used as an encapsulation layer to isolate the Al foil electrodes from the air. The testing samples were fixed on the force sensor in the impact system using double-sided adhesive tape for accurate pressure collection. An electrometer (6514, Keithley, USA) was connected to the two electrodes of the sample to measure the output charge and open-circuit voltage under impact. To test the piezoelectric response in bending, the strain sensor was attached to the polyimide substrate (Yingshida Co., Ltd., China) using double-sided tape, ensuring alignment with the substrate's center to maximize deformation. The two ends of the substrate were fixed on the linear motor's movable push plate and fixed plate, respectively. Different strains were applied by setting different propulsion steps of the linear motor. The open-circuit voltage was collected using an electrometer (6514, Keithley, USA). The strain calculation is illustrated in Supplementary Fig. 21.

The single-electrode method was used to test the voltage response of the samples under ultrasonic fields. For planar thin-film samples, the bottom electrode was connected to the positive electrode of the oscilloscope probe. For conduit samples, the films were tightly coiled onto a metallic needle (1.5 mm in diameter) to simulate a neural scaffold structure, while the needle was connected to the positive electrode of the oscilloscope probe. All samples were isolated from the test environment using polyimide tape. Ultrasonic (US) generation and characterization were performed with a commercial US transducer (DYW-1M, Yuzheng Co., Ltd., China) in DI water or under porcine skin (thickness: 5 mm, 12 mm and 17 mm). A power-supply system composed of a function generator (DG812, RIGOL, China) and a power amplifier (ATA-2012B, Aigtek, China) is utilized to provide a controllable driving voltage for the US (ultrasound) probe. The US transducer was positioned approximately 250 mm away from the samples. The voltage signals were measured and recorded using an oscilloscope (DSOX2012A, Keysight Technologies, USA) with a voltage probe (UTPO3, UNI-T Co., Ltd., China) with 40 M Ω input impedance. The US transducer and the negative pole of the oscilloscope probe were grounded to minimize noise.

Fabrication of biodegradable scaffold devices and strain sensors

The US-responsive biodegradable scaffold device consists of a PRSC inner layer and a PCL outer layer. The PRSC nanofiber film (thickness: about 11 μm) was rolled onto a 1.5 mm diameter metallic needle to create the 3D conduit structure. The electrospun non-aligned PCL nanofibers serve as the outer layer providing structural support. Specifically, PCL pellets (Mw = 80,000; Shanghai Yuanye Biotechnology

Co., Ltd., China) were dissolved in hexafluoroisopropanol (Shanghai Aladdin Biochemical Co., Ltd., China) at a 1:12.5 w/v ratio to obtain the electrospinning precursor solution. Electrospinning was performed under ambient conditions at 40% ± 10% relative humidity, using a 17-gauge needle with a solution feed rate of 0.1 mL/min and a collector rotation speed of 540 rpm. The needle tip-to-collector distance was maintained at ~10 cm, with an applied electric field of 16 kV. The resulting PCL fibers (~25 μm thickness) were vacuum-dried for more than 24 h to remove residual solvent. The PCL fibers were then wrapped around the PRSC conduit to achieve a biodegradable scaffold stimulator to promote nerve regeneration.

The strain sensor was composed of three main parts: the piezoelectric layer, electrode layers (upper and lower) and encapsulation layers (upper and lower). PRSC films were prepared as piezoelectric material layers, according to the previous description. Biodegradable molybdenum (Mo) foils (10 μm thickness) served as the electrode layers. For the encapsulation layer, a PLCL film (~100 μm thickness) was fabricated via solvent casting. PLCL pellets (LA:CL ratio = 50:50, intrinsic viscosity 2.7 dL g⁻¹; Jinan Daigang Biomaterial Co., Ltd., China) were dissolved in trichloromethane (CHCl₃; Beijing Tongguang Chemical Co., Ltd., China) at a 1:10 w/v ratio, followed by drop-casting and curing at 4 °C for 12 h to prevent bubble formation. The sensor patterns (the piezoelectric layer and electrode layers) were achieved using a laser cutting system (PR-U4, LPKF, Germany) operating at 1064 nm wavelength with 1.5 W power output. After laser processing, individual sensing channels were precisely aligned using an optical microscope, followed by edge sealing of the encapsulation layer with a manual hot press. The complete preparation process is shown in Supplementary Fig. 20.

Finite element analysis (FEA) simulations

The potential distribution in the film and conduit devices is simulated. In this model, the thickness of the devices is 50 μm, and the surrounding medium is water (with a relative permittivity, $\epsilon_r = 80$). The polarization is aligned with the z-axis. The lower surface of the film and the inner surface of the catheter are fixed and grounded. The power density of the US field is set at 1 W cm⁻². Normalized potentials are obtained using min-max normalization.

Cytotoxicity tests

The SH-SY5Y cell line (BNCC100158, BNCC, China) was seeded at optimal density onto laminin-coated PRSC, PLLA nanofibers, or TCP coverslips. The cells were stimulated daily using a low-power focused US probe (Chongqing Ronghai Co., Ltd., China) (1 MHz, 1 W/cm², 50% duty cycle) for 2 min over 3 days. To accurately determine the live/dead cell ratio, we performed flow cytometry as follows: SH-SY5Y cells after US stimulation were resuspended and centrifuged (350 g, 5 min) to remove the supernatant. The cells were then incubated with 7-AAD Viability Staining Solution (420403, BioLegend, USA) for 2 min before analysis by flow cytometry (Fortessa, BD, Franklin Lakes, USA). Each sample included three biological replicates ($n = 3$). The effect of piezoelectric stimulation on cell proliferation was assessed using the Cell-Light™ EdU Apollo In Vitro Kit (R1053.12, RIBBIO, China). After SH-SY5Y cells had fully adhered, the medium was replaced with SH-SY5Y complete medium containing 10 μM EdU, followed by daily 2-minute US stimulation for 3 days. Post-treatment samples were processed sequentially: fixed with 4% paraformaldehyde (G1101, Servicebio, China), autofluorescence quenched with glycine, and membranes permeabilized using Triton X-100 (T8200, Solarbio). EdU-positive cells were identified by Apollo 488 fluorescence staining (488 nm excitation) with nuclear counterstaining using Hoechst 33342. Images were captured using a confocal panoramic scanner at 488 nm excitation wavelength. Both total cell numbers and EdU+ cells were counted in each field of view. Each field contained at least 20 cells, with three clear fields randomly selected

for counting per well. Each experimental group included three biological replicates ($n = 3$).

Influence of PRSC on axonal growth under US stimulation

Spinal cord neuron isolation and culture following previously reported protocols¹⁰⁷. The cell suspension was cultured in Neurobasal medium (211103049, ThermoFisher Scientific, USA) supplemented with 2% B-27 (17504044, ThermoFisher Scientific), 1% GlutaMax (35050061, ThermoFisher Scientific), and 1% antibiotics on laminin-coated substrates (23017015, ThermoFisher Scientific). After 24–48 h of adhesion, the medium was replaced with induction medium containing 10 μM FUDR (F0503, Sigma-Aldrich) and uridine (U3003, Sigma-Aldrich). Following 72 h of induction, the medium was changed to passage medium (Neurobasal medium containing 2% B27, 1% GlutaMax-1, and 1% penicillin-streptomycin), and cells were stimulated daily using a low-power focused US probe (Chongqing Ronghai Co., Ltd., China) (1 MHz, 1 W cm⁻², 50% duty cycle) for 2 min over 3 days. To quantify neurite length, we performed β-tubulin immunofluorescence staining. Neuronal cultures were fixed with 4% paraformaldehyde (15 min at room temperature) and permeabilized with 0.1% Triton X-100 (10 min) to enable antibody penetration. A dual serum blocking system (10% goat serum (SL038, Solarbio) + 5% FBS (10100147 C, ThermoFisher Scientific)) containing 0.3 M glycine (A110749, Aladdin) was applied for 2 h to reduce nonspecific binding while neutralizing residual aldehydes. Anti-beta III tubulin antibody (clone 2G10, ab78078, Abcam, UK) was incubated overnight at 4 °C. The secondary antibody, Goat anti-Mouse IgG H&L (Alexa Fluor®488) pre-adsorbed antibody (1:200, ab150117, Abcam), was incubated at room temperature for 2 h. Nuclei were stained with DAPI (1:5000, ab285390, Abcam) for 15 min. Images were acquired using a confocal panoramic scanner (3DHISTECH, Panoramic Confocal, Hungary), and axon and dendrite lengths were measured using ImageJ (v1.54 f) with the NeuronJ (v1.4.3) plugin. The average neurite length per neuron was calculated. Quantitative analysis of axonal regeneration markers *Gap43* and *Galanin* transcription levels was performed using RT-qPCR following standard protocols¹⁰⁸. The primers for *Gap43* and *Galanin* were synthesized by Sangon Biotech (Wuhan) Co., Ltd., and their specific sequences are shown in Supplementary Table S2. The relative expression of *Gap43* and *Galanin* was calculated by normalizing the Ct value of each sample to that of *Gapdh*. Each experiment included three biological replicates ($n = 3$).

Influence of PRSC on calcium dynamics under US stimulation

SH-SY5Y cells were seeded onto PRSC, PLLA nanofibers, and TCP coverslips, respectively. After complete cell adhesion, cultures were washed with Tyrode's Solution (PB180338, Procell, China) for 5 min, followed by replacement with fresh Tyrode's Solution containing 10 μM Fluo-4 AM fluorescent probe (F14201, ThermoFisher Scientific). Cells were incubated at 37 °C for 30 min. The culture plate was then positioned on the stage of an ultra-resolution laser scanning confocal microscope (AI HD25, Nikon, Japan). Following focus stabilization, continuous imaging was acquired at 2-second intervals. After 120 s of baseline recording, US was applied (low-power focused US probe: 1 MHz, 1 W cm⁻², 50% duty cycle) while maintaining continuous imaging. Cellular fluorescence intensity was quantified using ImageJ (v1.54 f), and fluorescence bursts were counted. For calcium channel inhibition studies, SH-SY5Y cells were co-incubated with Fluo-4 AM and 50 μM Gd³⁺ (G489419, Aladdin) for 30 min following previous protocols^{109,110}. For mechanosensitive ion channel inhibition studies, SH-SY5Y cells were co-incubated with Fluo-4 AM and Gentamicin (20 mM, G302822, Aladdin) for 30 min following previous protocols¹¹¹.

Mechano-electrical nerve stimulation by PRSC composites

Female Sprague-Dawley (SD) rats were obtained from SPFbiotech (Beijing, China) and anesthetized via intraperitoneal injection of sodium pentobarbital (0.9%, 40 mg/kg, P3761, Sigma-Aldrich). Once

effective anesthesia was confirmed, the rats were sterilized, and the right sciatic nerve was fully exposed. The piezoelectric stimulator based on PRSC nanofilms, identical in structure to that used in the impact test, was fabricated. The electrodes at both ends of the device were connected through nerve stimulation electrodes, which were placed on the surface of the sciatic nerve. An electrical signal was generated by manually tapping the device, and activation of the gastrocnemius muscle was observed and recorded. Muscle activity during stimulation was monitored using a multi-channel electrophysiology acquisition and processing system (RM6240E/EC, Chengdu Instrument Factory, China). Recording electrodes were inserted into the gastrocnemius muscle to capture the compound muscle action potential (CMAP).

Animal studies for nerve regeneration using a piezoelectric scaffold stimulator

Over 50 eight-week-old female SD rats were randomly assigned to 7 groups (PCL US OFF, PCL US ON, PLLA US OFF, PLLA US ON, PRSC US OFF, PRSC US ON, Autograft US OFF) and anesthetized via intraperitoneal injection of sodium pentobarbital. Once anesthesia was confirmed, the rats were sterilized, and the right sciatic nerve was fully exposed. A 10 mm segment of the sciatic nerve was transected to create a nerve defect. Under a surgical microscope, grafts were sutured in each group without tension using 8-0 needle and thread. For nerve conduit suturing, both nerve stumps were inserted into the conduit with a 1 mm overlap and fixed in place. For autologous nerve transplantation, the excised 10 mm segment of sciatic nerve was reversed and sutured back in place. Following adequate hemostasis, the muscle layers and skin were closed sequentially using 4-0 surgical sutures. The incision site was disinfected with iodine, and the rats were monitored until recovery from anesthesia. After recovery, the rats were housed in groups according to the experimental design, with access to an automatic water supply and maintained under a 12-hour light/dark cycle. Beginning on the third day post-surgery, rats were blindfolded and placed on a platform with the right hind limb moderately secured for daily US treatment. This treatment involved low-power focused US probes (1 MHz, 1 W cm², 50% duty cycle, 20 min) and was administered for 14 consecutive days. Rats of the US OFF groups were exposed to the same procedures as those of the US ON groups, but with a deactivated US probe.

Gait analysis

Gait assessments were performed at 4, 8, and 12 weeks post-surgery using an automated gait analysis system (CatWalk XT, Noldus, Netherlands) to evaluate motor function recovery. Footprint data were collected from each experimental group ($n=5$), and the CatWalk XT 10.6 software (Noldus) was used to calculate the sciatic function index (SFI). The SFI was derived by analyzing footprints recorded as the animals walked freely across the platform, with emphasis on key parameters from both the injured (E) and uninjured (N) limbs. Measurements included toe spread (TS), intermediate toe spread (ITS), and paw length (PL). The SFI was then calculated using the Bain formula⁹:

$$\text{SFI} = -38.3 \times \left(\frac{\text{PL}_E - \text{PL}_N}{\text{PL}_N} \right) + 109.5 \times \left(\frac{\text{TS}_E - \text{TS}_N}{\text{TS}_N} \right) + 13.3 \times \left(\frac{\text{ITS}_E - \text{ITS}_N}{\text{ITS}_N} \right) - 8.8 \quad (2)$$

Electrophysiological evaluation

At 12 weeks post-surgery, the rats were weighed and anesthetized via intraperitoneal injection of sodium pentobarbital (30 mg/kg). A full dissection was performed to expose both the repaired sciatic nerve on

the right side and the intact sciatic nerve on the left. Using a multi-channel physiological signal recording and processing system (RM6240EC, Chengyi), stimulating electrodes were placed proximally to the graft without applying tension, and recording electrodes were inserted into the gastrocnemius muscle. A stimulation current of 3 mA was applied, and CMAPs were recorded in response to a single stimulation. The same procedure was repeated on the uninjured (left) side. For each subject in the group ($n=5$), the latency and peak amplitude ratio of the CMAP between the operated and control sides were calculated and analyzed.

Immunohistochemical and histological assessment

At 12 weeks postimplantation, the rats were humanely euthanized via an overdose of sodium pentobarbital. The regenerated sciatic nerve segments were then harvested and fixed in 4% paraformaldehyde, followed by dehydration in a 30% sucrose solution (powder, S112224, Aladdin). For immunofluorescence analysis, the tissues were embedded in O.C.T. Compound (Sakura Tissue-Tek, Torrance, USA) and cryosectioned transversely into 10 μm slices using a cryostat (CM1950, Leica, Germany). Additionally, regenerating nerves from rats at 4 weeks postimplantation were collected for longitudinal sectioning. Slides were initially incubated in blocking solution (10% goat serum, 5% fetal bovine serum, and 0.3 M glycine) for 2 h at room temperature. Subsequently, the tissue sections were incubated overnight at 4 °C with primary antibodies, including Rabbit Anti-S100 beta Monoclonal Antibody (Unconjugated, Clone EP1576Y, 1:200, ab52642, Abcam) and Mouse Monoclonal Anti-Neurofilament 200 (Phosphorylated and Non-Phosphorylated, 1:300, N0142, Sigma-Aldrich). Following three washes with PBS, the slides were incubated for 1 hour in the dark with secondary antibodies: Goat Anti-Rabbit IgG H&L (Alexa Fluor[®] 594, 1:200, ab150080, Abcam) and Goat Anti-Mouse IgG H&L (Alexa Fluor[®] 488, pre-adsorbed, 1:200, ab150117, Abcam). After a final series of PBS washes, the slides were counterstained with DAPI (1:5000, ab285390, Abcam) for 15 min, rinsed, and mounted with coverslips. Confocal images were acquired using a Panoramic Confocal Scanner (3DHISTECH), and image analysis was performed using ImageJ software (version 1.54 f).

To evaluate muscle atrophy, the gastrocnemius muscles were harvested by detaching them from the tendon. The muscles were then dried and weighed. Subsequent fixation, dehydration, and sectioning were performed as previously described. Muscle sections were stained using Masson's Trichrome Staining Kit (BA4079B, BASO, China) with the HistoCore SPECTRA ST + CV system (Leica). The stained slides were scanned using a panoramic confocal microscope, and the areas of muscle and collagen were quantified using Image-Pro Plus software (version 6.0).

To evaluate biocompatibility, hearts, livers, spleens, lungs and kidneys of rats were also harvested immediately after euthanasia. Samples were stained with HistoCore SPECTRA H&E Stain System S1 (3801654, Leica) using HistoCore SPECTRA ST + CV. The slides were then scanned using a panoramic confocal microscope. Data were obtained from five biological replicates ($n=5$).

TEM investigation of remyelinated nerve fibers

The ultrastructure of axons and myelin was examined using TEM. Nerve segments at the distal end were harvested and fixed in 4% paraformaldehyde with 2.5% glutaraldehyde (G1102, Servicebio) for 24 h. The samples were then post-fixed with 1% osmium tetroxide (OsO₄) (18456, Ted Pella Inc, USA) in 0.1 M PBS (pH 7.4) for 2 h at room temperature, followed by washing, dehydration, and embedding in EMBED 812 resin (90529-77-4, SPI, West Chester, USA). Ultra-thin transverse sections (50 nm) were prepared using a Leica UC7 ultramicrotome. The sections were then examined with a TEM (HITACHI HT7800). For each sample, five representative images were captured ($n=5$). Axon density, axon diameter, and myelin sheath thickness were measured

using ImageJ software (v1.54 f). The g-ratio was calculated using the formula: axon diameter/total fiber diameter.

Transcriptomic study of rats implanted with biodegradable scaffolds

Total RNA Extraction, cDNA Library Preparation, and Sequencing. 6-week-old female SD rats were randomly divided into two groups (PCL US OFF group and PRSC US ON group, $n = 3$). US parameters were as described in the previous section, and the treatment lasted for 12 days. Apart from the US treatment, both groups were housed under identical conditions. At 3 weeks post-injury, the rats were euthanized, and the regenerated tissue within the nerve conduits on the injured side was collected. The tissue was washed with PBS to remove blood clots, and total RNA was extracted immediately using Trizol (15596018 C, ThermoFisher Scientific) and assessed using the Agilent 2100 BioAnalyzer (Agilent Technologies, USA) and Qubit Fluorometer (ThermoFisher Scientific). Samples meeting the following criteria were used for subsequent experiments: RNA Integrity Index (RNI) > 7.0 and 28S:18S ratio > 1.8. RNA-seq libraries were generated and sequenced by Biomarker Technologies Corporation (Beijing, China). Independent libraries were constructed for each of the 3 replicate samples, and sequencing and analysis were conducted using the NEB Next Ultra RNA Library Prep Kit (NEB). The final libraries were quantified using the KAPA Library Quantification Kit (KAPA Biosystems, South Africa) and Agilent 2100 BioAnalyzer. After quantitative RT-PCR validation, paired-end sequencing with a read length of 150 base pairs was performed using the Illumina NovaSeq sequencer (Illumina, USA).

RNA-seq data analysis

The sequencing data were analyzed using the human genome assembly hg38 as the reference genome. The quality of the sequencing reads was assessed using FastQC (v0.11.2), and low-quality data were filtered using fastp (v0.14.0). The filtered raw data were aligned to the reference genome using HISAT2 (v2.2.0) with default parameters. Processed data from each sample were aligned to the reference genome using HISAT2. Gene expression analysis was performed using StringTie (v2.2.1). Differential gene expression (DEG) analysis was conducted using Limma (v3.32.10) and DESeq (v1.28.0). Genes with fold changes > 2 and p values < 0.05 were identified as differentially expressed. GO enrichment analysis of the DEGs was performed using the Gene Ontology (GO) database and the R package “clusterProfiler” (v4.4.0, <https://github.com/YuLab-SMU/clusterProfiler>)¹². Pathway enrichment analysis of DEGs was conducted using the Kyoto Encyclopedia of Genes and Genomes (KEGG) and the “clusterProfiler” package. Additionally, gene set enrichment analysis (GSEA) (v4.1.0, <http://www.gsea-msigdb.org/gsea/downloads.jsp>) was performed to further determine gene sets with clear functional relevance.

Animal studies for intestinal motility monitoring using biodegradable strain sensors

Over ten 2-year-old New Zealand White rabbits were obtained, and body weights were recorded. Anesthesia was induced via intraperitoneal injection of sodium pentobarbital (0.5 mL kg⁻¹) and maintained using vaporized isoflurane (1.5–2% in oxygen). Rabbits were placed in a supine position, and standard surgical preparation was performed, including abdominal fur removal and aseptic disinfection. A midline laparotomy was conducted to expose the intestines. The strain sensor was attached to the surface of the colon using a previously developed biodegradable adhesive hydrogel. After implantation, the intestines were repositioned within the abdominal cavity, and the abdominal wall was closed in layers using 2-0 surgical sutures. Rabbits in the pharmacological intervention group received oral administration of domperidone (0.5 g kg⁻¹) one hour prior to implantation, to accelerate intestinal motility, accompanied by ad libitum access to water to enhance systemic absorption. In the ischemia group, Mesenteric

ischemic enteropathy was modeled via selective arterial ligation, using 2-0 sutures to occlude the arterial supply to the targeted colonic segment. Successful induction of ischemia was confirmed by visual identification of darkened vasculature distal to the ligation site. Following implantation, rabbits were maintained in the supine position while colonic peristaltic activity was continuously monitored using an implantable wireless telemetry module.

Blood samples from New Zealand White rabbits were collected at two time points: prior to surgery and after the completion of peristaltic signal acquisition. Venous blood was obtained via marginal ear vein puncture using sterile syringes under aseptic conditions. The samples were immediately transferred into EDTA-K3 anticoagulant-containing vacuum collection tubes (BD Vacutainer®) and gently inverted 8–10 times to ensure thorough mixing with the anticoagulant, thereby preventing coagulation and hemolysis.

Within 2 h of collection, the samples were centrifuged (1500 g, 15 min) at 4 °C to separate plasma. Quantitative analysis of inflammatory cytokines, including interleukin-6 (IL-6) and tumor necrosis factor-alpha (TNF- α), was performed using commercial ELISA kits (TNF- α assay kit HO52-1-2 and IL-6 assay kit HO07-1-2, Nanjing Jiancheng Bioengineering Institute, China).

Following the peristaltic monitoring, the rabbits were humanely euthanized via intravenous injection of 20 mL of air, followed by immediate laparotomy. Targeted colonic segments (~2 cm) were harvested within 3 min post-mortem to minimize autolytic changes. Tissue samples were stained using the HistoCore SPECTRA H&E Stain System S1 (3801654, Leica) with the HistoCore SPECTRA ST + CV platform. The stained slides were subsequently scanned using a panoramic confocal microscope ($n = 5$).

Signal processing based on the EMD algorithm

The acquired raw colonic peristalsis signals were adaptively decomposed into multiple intrinsic mode functions (IMFs) using the Empirical Mode Decomposition (EMD) algorithm implemented in MATLAB R2022b. Each IMF captured distinct frequency components at different temporal scales within the original signal. To assess the spectral-temporal characteristics of the individual IMFs, a short-time Fourier transform (STFT) was subsequently applied, enabling detailed analysis of their time-frequency distributions.

Statistical analysis

Statistical analyses were performed using SPSS software (version 26.0), with two-sided independent-samples t-test used for two-group comparisons, and one-way ANOVA Tukey test (two-sided) for multiple-group comparisons (* $P < 0.05$, ** $P < 0.01$, *** $P < 0.001$ and **** $P < 0.0001$). Statistical significance of pairwise comparisons not denoted on the graphs corresponds to $P > 0.05$ (not significant), unless otherwise specified. Data are presented as box plots, where the center line indicates the median, the box edges represent the first and third quartiles, and the whiskers extend to the smallest and largest values within 1.5 times the interquartile range.

Ethics

Experiments involving animals have been carried out in accordance with a protocol approved by an ethics committee. Specifically, all experimental protocols received approval from the Experimental Animal Ethics Committee of PLA General Hospital (approval number: 2023-x19-79) and Beijing Institute of Traumatology and Orthopedics (approval number: 2023-12-01). All animal-related procedures were conducted in accordance with the institutional guidelines of PLA General Hospital and the Beijing Institute of Traumatology and Orthopedics.

Reporting summary

Further information on research design is available in the Nature Portfolio Reporting Summary linked to this article.

Data availability

Gene expression data have been deposited in the Gene Expression Omnibus (GEO) with the accession code GSE313757 (<https://www.ncbi.nlm.nih.gov/geo/query/acc.cgi>). All data supporting the findings of this study are available within the article and its supplementary files. Any additional requests for information can be directed to, and will be fulfilled by, the corresponding authors. Source data are provided with this paper.

References

- Zhang, T. et al. Piezoelectric ultrasound energy-harvesting device for deep brain stimulation and analgesia applications. *Sci. Adv.* **8**, eabk0159 (2022).
- Zhang, Y. et al. Self-powered pacemaker based on all-in-one flexible piezoelectric nanogenerator. *Nano Energy* **99**, 107420 (2022).
- Han, M. et al. Three-dimensional piezoelectric polymer micro-systems for vibrational energy harvesting, robotic interfaces and biomedical implants. *Nat. Electron.* **2**, 26–35 (2019).
- Cai, L. et al. Piezoelectric metal-organic frameworks based sonosensitizer for enhanced nanozyme catalytic and sonodynamic therapies. *Acs Nano* **17**, 7901–7910 (2023).
- Fan, Y. et al. Biomimetic piezoelectric nanomaterial-modified oral microrobots for targeted catalytic and immunotherapy of colorectal cancer. *Sci. Adv.* **10**, eadm9561 (2024).
- Zhou, S. et al. Injectable ultrasound-powered bone-adhesive nanocomposite hydrogel for electrically accelerated irregular bone defect healing. *J. Nanobiotechnology* **22**, 54 (2024).
- Pi, W. et al. Sono-electro-mechanical therapy for peripheral nerve regeneration through piezoelectric nanotracts. *Nano Today* **50**, 101860 (2023).
- Xu, Q. Q. et al. Construction of bio-piezoelectric platforms: from structures and synthesis to applications. *Adv. Mater.* **33**, 2008452 (2021).
- Chen, X.-Z. et al. Hybrid magnetoelectric nanowires for nanorobotic applications: fabrication, magnetoelectric coupling, and magnetically assisted in vitro targeted drug delivery. *Adv. Mater.* **29**, 1605458 (2017).
- Mushtaq, F. et al. Motile piezoelectric nanoels for targeted drug delivery. *Adv. Funct. Mater.* **29**, 1808135 (2019).
- Tang, C. et al. Unconstrained piezoelectric vascular electronics for wireless monitoring of hemodynamics and cardiovascular health. *Small* **20**, 2304752 (2024).
- Chang, G. et al. PVDF/ZnO piezoelectric nanofibers designed for monitoring of internal micro-pressure. *Rsc Adv.* **14**, 11775–11783 (2024).
- Cung, K. et al. Biotemplated synthesis of PZT nanowires. *Nano Lett.* **13**, 6197–6202 (2013).
- Rodel, J. et al. Transferring lead-free piezoelectric ceramics into application. *J. Eur. Ceram. Soc.* **35**, 1659–1681 (2015).
- Marino, A., Battaglini, M., De Pasquale, D., Degl'Innocenti, A. & Ciofani, G. Ultrasound-activated piezoelectric nanoparticles inhibit proliferation of breast cancer cells. *Sci. Rep.-Uk* **8**, 6257 (2018).
- Su, R. et al. Nano-ferroelectric for high efficiency overall water splitting under ultrasonic vibration. *Angew. Chem. Int. Ed.* **58**, 15076–15081 (2019).
- Jeong, C. K. et al. Virus-directed design of a flexible BaTiO₃ nanogenerator. *Acs Nano* **7**, 11016–11025 (2013).
- Wang, Y. et al. Synthesis of cubic LiNbO₃ nanoparticles and their application in vitro bioimaging. *Appl. Phys. a-Mater.* **117**, 2121–2126 (2014).
- Yu, S. W., Kuo, S. T., Tuan, W. H., Tsai, Y. Y. & Wang, S. F. Cytotoxicity and degradation behavior of potassium sodium niobate piezoelectric ceramics. *Ceram. Int* **38**, 2845–2850 (2012).
- Wu, P. et al. Ultrasound-driven electrical stimulation based on biodegradable piezoelectric nanogenerators for enhancing and monitoring the nerve tissue repair. *Nano Energy* **102**, 107707 (2022).
- Li, Q. & Wang, Q. Ferroelectric polymers and their energy-related applications. *Macromol. Chem. Phys.* **217**, 1228–1244 (2016).
- Wan, C. Y. & Bowen, C. R. Multiscale-structuring of polyvinylidene fluoride for energy harvesting: the impact of molecular-, micro- and macro-structure. *J. Mater. Chem. A* **5**, 3091–3128 (2017).
- Chorsi, M. T. et al. Piezoelectric biomaterials for sensors and actuators. *Adv. Mater.* **31**, 1802084 (2019).
- Guerin, S. et al. Control of piezoelectricity in amino acids by supramolecular packing. *Nat. Mater.* **17**, 180 (2018).
- Hamilton, B. D., Hillmyer, M. A. & Ward, M. D. Glycine polymorphism in nanoscale crystallization chambers. *Cryst. Growth Des.* **8**, 3368–3375 (2008).
- Guerin, S. et al. Racemic amino acid piezoelectric transducer. *Phys. Rev. Lett.* **122**, 047701 (2019).
- Vasilev, S. et al. Piezoelectric properties of diphenylalanine microtubes prepared from the solution. *J. Phys. Chem. Solids* **93**, 68–72 (2016).
- Amdursky, N., Beker, P., Schklovsky, J., Gazit, E. & Rosenman, G. Ferroelectric and related phenomena in biological and bioinspired nanostructures. *Ferroelectrics* **399**, 107–117 (2010).
- Tao, Z. et al. Diphenylalanine-based degradable piezoelectric nanogenerators enabled by polylactic acid polymer-assisted transfer. *Nano Energy* **88**, 106229 (2021).
- Yucel, T., Cebe, P. & Kaplan, D. L. Structural origins of silk piezoelectricity. *Adv. Funct. Mater.* **21**, 779–785 (2011).
- Zhou, Z., Qian, D. & Minary-Jolandan, M. Molecular mechanism of polarization and piezoelectric effect in super-twisted collagen. *Acs Biomater. Sci. Eng.* **2**, 929–936 (2016).
- Sierra, D. L. G. et al. Flexible piezoelectric chitosan and barium titanate biocomposite films for sensor applications. *Eur. J. Inorg. Chem.* **2021**, 792–803 (2021).
- Jacob, J., More, N., Kalia, K. & Kapusetti, G. Piezoelectric smart biomaterials for bone and cartilage tissue engineering. *Inflamm. Regen.* **38**, 2 (2018).
- Hoque, N. A. et al. Biowaste crab shell-extracted chitin nanofiber-based superior piezoelectric nanogenerator. *J. Mater. Chem. A* **6**, 13848–13858 (2018).
- Csoka, L. et al. Piezoelectric effect of cellulose nanocrystals thin films. *Acs Macro Lett.* **1**, 867–870 (2012).
- Ghosh, S. K. et al. Fully biodegradable hierarchically designed high-performance nanocellulose piezo-arrays. *Sci. Adv.* **11**, eads0778 (2025).
- Ochiai, T. & Fukada, E. Electromechanical properties of poly-L-lactic acid. *Jpn J. Appl. Phys.* **37**, 3374–3376 (1998).
- Li, T. et al. Ultrastable piezoelectric biomaterial nanofibers and fabrics as an implantable and conformal electromechanical sensor patch. *Sci. Adv.* **10** <https://doi.org/10.1126/sciadv.adn8706> (2024).
- Fukada, E. History and recent progress in piezoelectric polymers. *Ieee T Ultrason Ferr.* **47**, 1277–1290 (2000).
- Dai, F., Geng, Q., Hua, T., Sheng, X. & Yin, L. Organic biodegradable piezoelectric materials and their potential applications as bioelectronics. *Soft Sci.* **3**, 7 (2023).
- Liu, Y. et al. Biomimetic electroactive materials and devices for regenerative engineering. *Nat. Rev. Electr. Eng.* **2**, 188–204 (2025).
- Curry, E. J. et al. Biodegradable piezoelectric force sensor. *P Natl. Acad. Sci.* **115**, 909–914 (2018).
- Curry, E. J. et al. Biodegradable nanofiber-based piezoelectric transducer. *P Natl. Acad. Sci.* **117**, 214–220 (2020).

44. Chorsi, M. T. et al. Highly piezoelectric, biodegradable, and flexible amino acid nanofibers for medical applications. *Sci. Adv.* **9**, eadg6075 (2023).
45. Nguyen, V., Zhu, R., Jenkins, K. & Yang, R. S. Self-assembly of diphenylalanine peptide with controlled polarization for power generation. *Nat. Commun.* **7**, 13566 (2016).
46. Li, X. et al. One-step high-speed thermal-electric aerosol printing of piezoelectric bio-organic films for wirelessly powering bioelectronics. *Sci. Adv.* **10**, eadq3195 (2024).
47. Yang, F. et al. Wafer-scale heterostructured piezoelectric bio-organic thin films. *Science* **373**, 337 (2021).
48. Xue, H. Y. et al. Flexible, biodegradable ultrasonic wireless electrotherapy device based on highly self-aligned piezoelectric biofilms. *Sci. Adv.* **10**, eadn0260 (2024).
49. Zhang, H. Y. et al. Biodegradable ferroelectric molecular crystal with large piezoelectric response. *Science* **383**, 1492–1498 (2024).
50. Valasek, J. Piezo-electric and allied phenomena in rochelle salt. *Phys. Rev.* **17**, 475–481 (1921).
51. Levitskii, R. R., Zachek, I. R., Verkholiyak, T. M. & Moina, A. P. Dielectric, piezoelectric, and elastic properties of the Rochelle salt $\text{NaKC}_4\text{H}_4\text{O}_6 \cdot 4\text{H}_2\text{O}$: A theory. *Phys. Rev. B* **67**, 174112 (2003).
52. Mason, W. P. A dynamic measurement of the elastic, electric and piezoelectric constants of rochelle salt. *Phys. Rev.* **55**, 775–789 (1939).
53. Lemaire, E., Ayela, C. & Atli, A. Eco-friendly materials for large area piezoelectronics: self-oriented Rochelle salt in wood. *Smart Mater. Struct.* **27**, 025005 (2018).
54. Garemark, J. et al. Salt-In-Wood Piezoelectric Power Generators with Circular Materials Design for High-Performance Sustainable Energy Harvesting. *Adv. Funct. Mater.* 2418454 (2025).
55. Lemaire, E., Moser, R., Borsa, C. J. & Briand, D. Green paper-based piezoelectronics for sensors and actuators. *Sens. Actuat a-Phys.* **244**, 285–291 (2016).
56. Lemaire, E., Thuau, D., De Vaulx, J. B., Vaissiere, N. & Atilla, A. Rochelle Salt-Based Ferroelectric and Piezoelectric Composite Produced with Simple Additive Manufacturing Techniques. *Mater.* **14**, 6132 (2021).
57. He, Q. Q. et al. Growing recyclable and healable piezoelectric composites in 3D printed bioinspired structure for protective wearable sensor. *Nat. Commun.* **14**, 6477 (2023).
58. Shyju, T. S., Anandhi, S. & Gopalakrishnan, R. Comparative studies on conventional solution and Sankaranarayanan-Ramasamy (SR) methods grown potassium sodium tartrate tetrahydrate single crystals. *Crystengcomm* **14**, 1387–1396 (2012).
59. Lu, L. J., Ding, W. Q., Liu, J. Q. & Yang, B. Flexible PVDF based piezoelectric nanogenerators. *Nano Energy* **78**, 105251 (2020).
60. Chen, X. et al. High-performance piezoelectric nanogenerators with imprinted p(vdf-trfe)/batio3 nanocomposite micropillars for self-powered flexible sensors. *Small* **13**, 1604245 (2017).
61. Owusu, F., Venkatesan, T. R., Nüesch, F. A., Negri, R. M. & Opris, D. M. How to Make Elastomers Piezoelectric? *Adv. Mater. Technol.-Us* **8**, 00099 (2023).
62. Rajala, S. et al. Cellulose nanofibril film as a piezoelectric sensor material. *Acs Appl Mater. Inter* **8**, 15607–15614 (2016).
63. de Marzo, G. et al. Sustainable, flexible, and biocompatible enhanced piezoelectric chitosan thin film for compliant piezo-sensors for human health. *Adv. Electron Mater.* **9**, 2200069 (2022).
64. Ghosh, S. K., Park, J., Na, S., Kim, M. P. & Ko, H. A fully biodegradable ferroelectric skin sensor from edible porcine skin gelatine. *Adv. Sci.* **8**, 2005010 (2021).
65. Kim, K. et al. Biodegradable, electro-active chitin nanofiber films for flexible piezoelectric transducers. *Nano Energy* **48**, 275–283 (2018).
66. Li, T. et al. Soft ferroelectret ultrasound receiver for targeted peripheral neuromodulation. *Nat. Commun.* **14**, 8386 (2023).
67. Genchi, G. G. et al. P(VDF-TrFE)/BaTiO₃ Nanoparticle Composite Films Mediate Piezoelectric Stimulation and Promote Differentiation of SH-SY5Y Neuroblastoma Cells. *Adv. Health. Mater.* **5**, 1808–1820 (2016).
68. Marino, A. et al. Piezoelectric nanoparticle-assisted wireless neuronal stimulation. *Acs Nano* **9**, 7678–7689 (2015).
69. Chu, X. L. et al. Basic mechanisms of peripheral nerve injury and treatment via electrical stimulation. *Neural Regen. Res* **17**, 2185–2193 (2022).
70. Gordon, T. Electrical stimulation to enhance axon regeneration after peripheral nerve injuries in animal models and humans. *Neurotherapeutics* **13**, 295–310 (2016).
71. Xu, K. L. et al. Effect of Electrical and Electromechanical Stimulation on PC12 Cell Proliferation and Axon Outgrowth. *Front Bioeng. Biotech.* **9**, 757906 (2021).
72. Chung, D. Y., Shum, A. & Caraveo, G. GAP-43 and BASP1 in axon regeneration: implications for the treatment of neurodegenerative diseases. *Front Cell Dev. Biol.* **8**, 567537 (2020).
73. Shin, J. E. & Cho, Y. Epigenetic regulation of axon regeneration after neural injury. *Mol. Cells* **40**, 10–16 (2017).
74. Xu, X. F. et al. Galanin and its receptor system promote the repair of injured sciatic nerves in diabetic rats. *Neural Regen. Res* **11**, 1517–1526 (2016).
75. Kalil, K., Li, L. & Hutchins, B. I. Signaling mechanisms in cortical axon growth, guidance, and branching. *Front Neuroanat.* **5**, 62 (2011).
76. Markworth, R. et al. Sensory Axon Growth Requires Spatiotemporal Integration of CaSR and TrkB Signaling. *J. Neurosci.* **39**, 5842–5860 (2019).
77. Xi, F. et al. Calcium/calmodulin-dependent protein kinase II regulates mammalian axon growth by affecting F-actin length in growth cone. *J. Cell Physiol.* **234**, 23053–23065 (2019).
78. Yan, X. D. et al. Electrical Stimulation Induces Calcium-Dependent Neurite Outgrowth and Immediate Early Genes Expressions of Dorsal Root Ganglion Neurons. *Neurochem Res* **39**, 129–141 (2014).
79. Javeed, S., Faraji, A. H., Dy, C., Ray, W. Z. & MacEwan, M. R. Application of electrical stimulation for peripheral nerve regeneration: Stimulation parameters and future horizons. *Interdiscip. Neurosurg.* **24**, 101117 (2021).
80. Gordon, T., Amirjani, N., Edwards, D. C. & Chan, K. M. Brief post-surgical electrical stimulation accelerates axon regeneration and muscle reinnervation without affecting the functional measures in carpal tunnel syndrome patients. *Exp. Neurol.* **223**, 192–202 (2010).
81. Koo, J. et al. Wireless bioresorbable electronic system enables sustained nonpharmacological neuroregenerative therapy. *Nat. Med.* **24**, 1830–1836 (2018).
82. Wang, L. et al. A fully biodegradable and self-electrified device for neuroregenerative medicine. *Sci. Adv.* **6**, eabc6686 (2020).
83. Golovachev, N. et al. Metabolic-driven analytics of traumatic brain injury and neuroprotection by ethyl pyruvate. *J. Neuroinflamm.* **21**, 294 (2024).
84. Bala, C., Rusu, A., Ciobanu, D. M., Roman, G. & Craciun, A. E. Metabolomics in Pathogenic Pathways and Targeted Therapies for Diabetic Neuropathy: A Comprehensive Review. *Metabolites* **15**, 86 (2025).
85. Yang, Y. H., Lei, L., Bao, Y. P. & Zhang, L. An integrated metabolomic screening platform discovers the potential biomarkers of ischemic stroke and reveals the protective effect and mechanism of folic acid. *Front Mol. Biosci.* **9**, 783793 (2022).
86. Handlogten, M. E., Huang, C. F., Shiraishi, N., Awata, H. & Miller, R. T. The Ca²⁺-sensing receptor activates cytosolic phospholipase A2

- via a Gqalpha-dependent ERK-independent pathway. *J. Biol. Chem.* **276**, 13941–13948 (2001).
87. Sundaram, V. K. et al. Adipo-glia signaling mediates metabolic adaptation in peripheral nerve regeneration. *Cell Metab.* **35**, 2136–2152.e2139 (2023).
 88. Meitzen, J., Luoma, J. I., Stern, C. M. & Mermelstein, P. G. β 1-Adrenergic receptors activate two distinct signaling pathways in striatal neurons. *J. Neurochemistry* **116**, 984–995 (2011).
 89. Al-Majed, A. A., Brushart, T. M. & Gordon, T. Electrical stimulation accelerates and increases expression of BDNF and trkB mRNA in regenerating rat femoral motoneurons. *Eur. J. Neurosci.* **12**, 4381–4390 (2000).
 90. Ben-Ari, Y. Excitatory actions of gaba during development: the nature of the nurture. *Nat. Rev. Neurosci.* **3**, 728–739 (2002).
 91. Chu, X.-L. et al. Basic mechanisms of peripheral nerve injury and treatment via electrical stimulation. *Neural Regen Res* **17**, <https://doi.org/10.4103/1673-5374.335823> (2022).
 92. Patel, A., Kaleya, R. N. & Sammartano, R. J. Pathophysiology of Mesenteric Ischemia. *Surgical Clin. North Am.* **72**, 31–41 (1992).
 93. Bala, M. et al. Acute mesenteric ischemia: guidelines of the World Society of Emergency Surgery. *World J. Emerg. Surg.* **12**, 38 (2017).
 94. Kassahun, W. T., Schulz, T., Richter, O. & Hauss, J. Unchanged high mortality rates from acute occlusive intestinal ischemia: six year review. *Langenbeck's Arch. Surg.* **393**, 163–171 (2008).
 95. Bradbury, A. W., Brittenden, J., McBride, K. & Ruckley, C. V. Mesenteric ischaemia: A multidisciplinary approach. *Br. J. Surg.* **82**, 1446–1459 (1995).
 96. Liu, S. N. et al. A Biodegradable, adhesive, and stretchable hydrogel and potential applications for allergic rhinitis and epistaxis. *Adv. Health. Mater.* <https://doi.org/10.1002/adhm.202302059> (2023).
 97. Li, P., Kreikemeier-Bower, C., Xie, W., Kothari, V. & Terry, B. S. Design of a wireless medical capsule for measuring the contact pressure between a capsule and the small intestine. *J. Biomech. Eng.* <https://doi.org/10.1115/1.4036260> (2017).
 98. Sarna, S. K. Physiology and pathophysiology of colonic motor activity. *Digestive Dis. Sci.* **36**, 827–862 (1991).
 99. Benabdallah, H., Messaoudi, D. & Gharzouli, K. The spontaneous mechanical activity of the circular smooth muscle of the rabbit colon in vitro. *Pharmacol. Res.* **57**, 132–141 (2008).
 100. McKirdy, H. C. *Factors influencing the movements of the distal colon of the rabbit*, University of Glasgow (United Kingdom), (1970).
 101. Javeed, S., Faraji, A. H., Dy, C., Ray, W. Z. & MacEwan, M. R. Application of electrical stimulation for peripheral nerve regeneration: Stimulation parameters and future horizons. *Interdiscip. Neurosurg.* <https://doi.org/10.1016/j.inat.2021.101117> (2021).
 102. Li, X. et al. Electrical stimulation accelerates Wallerian degeneration and promotes nerve regeneration after sciatic nerve injury. *Glia* **71**, 758–774 (2023).
 103. Zuo, K. J., Gordon, T., Chan, K. M. & Borschel, G. H. Electrical stimulation to enhance peripheral nerve regeneration: Update in molecular investigations and clinical translation. *Exp. Neurol.* **332**, 113397 (2020).
 104. Henley, J. & Poo, M. -m Guiding neuronal growth cones using Ca²⁺ signals. *Trends Cell Biol.* **14**, 320–330 (2004).
 105. Yang, F. et al. Manufacturing and morphology structure of polylactide-type microtubules orientation-structured scaffolds. *Biomaterials* **27**, 4923–4933 (2006).
 106. Li, W. et al. Delineating complex ferroelectric domain structures via second harmonic generation spectral imaging. *J. Materiomics* **9**, 395–402 (2023).
 107. Ruan, Y. et al. Calycosin activates Nrf2/Keap1 signaling to ameliorate hydrogen peroxide-induced spinal cord neuron death and mitochondrial dysfunction. *J. Biochem Mol. Toxic.* **38**, e23808 (2024).
 108. Zucha, D., Kubista, M. & Valihrach, L. Tutorial: guidelines for single-cell RT-qPCR. *Cells-Basel* **10**, 2607 (2021).
 109. Fan, C. H. et al. Selective activation of cells by piezoelectric molybdenum disulfide nanosheets with focused ultrasound. *ACS Nano* **17**, 9140–9154 (2023).
 110. Cho, M. R., Thatte, H. S., Silvia, M. T. & Golan, D. E. Transmembrane calcium influx induced by ac electric fields. *Faseb J.* **13**, 677–683 (1999).
 111. Jacques-Fricke, B. T., Seow, Y. Q., Gottlieb, P. A., Sachs, F. & Gomez, T. M. Ca²⁺ influx through mechanosensitive channels inhibits neurite outgrowth in opposition to other influx pathways and release from intracellular stores. *J. Neurosci.* **26**, 5656–5664 (2006).
 112. Yu, G. C., Wang, L. G., Han, Y. Y. & He, Q. Y. clusterProfiler: an R Package for Comparing Biological Themes Among Gene Clusters. *Omic* **16**, 284–287 (2012).

Acknowledgements

The project was supported by the National Natural Science Foundation of China (32571534 to L.Y.), Tsinghua-Toyota Joint Research Fund (to L.Y.), Beijing Natural Science Foundation (L254019), the National Natural Science Foundation of China (T2425003 and 52272277 to X.S.), Tsinghua University Initiative Scientific Research Program (2024Z02ORD001, to X.S.), and Beijing Municipal Natural Science Foundation (Z220015 to L.Y., L222147 to Y.W.).

Author contributions

F.D. and L.Y. conceived the idea. F.D. and Honglai C. performed material design, fabrication and characterization. H.D., Q.W., and F.D. performed the design and characterization of the programmable ultrasound system. F.Y. and M.Z. performed the design, fabrication, and characterization of the wireless transmission module. F.D., Haofeng C., and L.Y. designed and performed cell experiments. F.D., Haofeng C., T.S., Y.G., Y.C., J.M., Honglai C, and L.Y. designed and performed biological experiments on sciatic nerve regeneration. F.D., H.Q., L.T., Y.J., L.C., and L.Y. designed and performed biological experiments on colon peristalsis monitoring. S.W., W.L., T.F., S.L., B.Y., C.Y., A.A., H.Q., H.D., Honglai C., Haofeng C., F.D., and L.Y. participated in the data analysis discussion. F.D., Q.L., J.L., M.Z., C.M., L.T., J.P., Y.W., X.S., and L.Y. provided tools and supervised the research. F.D., Haofeng C., and L.Y. wrote the paper in consultation with the rest of the authors.

Competing interests

The authors declare no competing interests.

Additional information

Supplementary information The online version contains supplementary material available at <https://doi.org/10.1038/s41467-026-68930-2>.

Correspondence and requests for materials should be addressed to Lei Tian, Jun Zhang, Yu Wang or Lan Yin.

Peer review information *Nature Communications* thanks the anonymous reviewer(s) for their contribution to the peer review of this work. A peer review file is available.

Reprints and permissions information is available at <http://www.nature.com/reprints>

Publisher's note Springer Nature remains neutral with regard to jurisdictional claims in published maps and institutional affiliations.

Open Access This article is licensed under a Creative Commons Attribution-NonCommercial-NoDerivatives 4.0 International License, which permits any non-commercial use, sharing, distribution and reproduction in any medium or format, as long as you give appropriate credit to the original author(s) and the source, provide a link to the Creative Commons licence, and indicate if you modified the licensed material. You do not have permission under this licence to share adapted material derived from this article or parts of it. The images or other third party material in this article are included in the article's Creative Commons licence, unless indicated otherwise in a credit line to the material. If material is not included in the article's Creative Commons licence and your intended use is not permitted by statutory regulation or exceeds the permitted use, you will need to obtain permission directly from the copyright holder. To view a copy of this licence, visit <http://creativecommons.org/licenses/by-nc-nd/4.0/>.

© The Author(s) 2026

¹School of Materials Science and Engineering, Tsinghua University, Beijing, P. R. China. ²The Key Laboratory of Advanced Materials of Ministry of Education, Tsinghua University, Beijing, P. R. China. ³School of Medicine, Nankai University, Tianjin, P. R. China. ⁴Institute of Orthopedics, Chinese PLA General Hospital, Beijing, P. R. China. ⁵Beijing Key Lab of Regenerative Medicine in Orthopedics, Chinese PLA General Hospital, Beijing, P. R. China. ⁶Key Laboratory of Musculoskeletal Trauma and Injuries PLA, Chinese PLA General Hospital, Beijing, P. R. China. ⁷Department of Neurosurgery, the First Medical Centre, Chinese PLA General Hospital, Beijing, P. R. China. ⁸Laboratory of Musculoskeletal Regenerative Medicine, Beijing Institute of Traumatology and Orthopaedics, Beijing, P. R. China. ⁹Weiyang College, Tsinghua University, Beijing, P. R. China. ¹⁰Department of Electronic Engineering, Tsinghua University, Beijing, P. R. China. ¹¹Beijing National Research Center for Information Science and Technology, Tsinghua University, Beijing, P. R. China. ¹²Institute for Precision Medicine, Tsinghua University, Beijing, P. R. China. ¹³Institute of Intelligent Healthcare, Tsinghua University, Beijing, P. R. China. ¹⁴TsingPAI Technology Co., Ltd., Beijing, P. R. China. ¹⁵State Key Laboratory of New Ceramics and Fine Processing, Tsinghua University, Beijing, P. R. China. ¹⁶IDG/McGovern Institute for Brain Research, Tsinghua University, Beijing, P. R. China. ¹⁷State Key Laboratory of Flexible Electronics Technology, Tsinghua University, Beijing, P. R. China. ¹⁸Department of Cardiovascular Surgery, The ninth Medical Center, Chinese PLA General Hospital, Beijing, P.R. China. ¹⁹These authors contributed equally: Fanqi Dai, Haofeng Cheng, Hui Qi. ✉ e-mail: tianmushroom@163.com; zhangjun@301hospital.com.cn; wangyu@301hospital.com.cn; lanyin@tsinghua.edu.cn